Renewable Energy 254 (2025) 123555

Contents lists available at ScienceDirect

Renewable Energy

journal homepage: www.elsevier.com/locate/renene

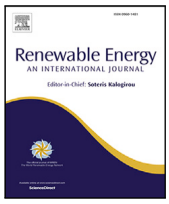

# Modal dynamics of wind turbine wake meandering from lidar observations

Nicholas Hamilton *, Paula Doubrawa, Patrick Moriarty, Stefano Letizia, Regis Thedin

*National Renewable Energy Laboratory (NREL), Golden, CO, USA*

ARTICLE INFO

*Keywords:*
Wind turbine wake meandering
Proper orthogonal decomposition
Lidar

ABSTRACT

Horizontal scans from nacelle-mounted lidars provide time series measurements of wind turbine wakes across diverse atmospheric conditions, enabling analysis of coherent turbulent structures that influence wake meandering through proper orthogonal decomposition (POD). While low-order modes capture the most energetic turbulent structures, our analysis reveals that they do not necessarily dominate wake meandering dynamics. We evaluate more than 16,000 combinatorial reconstructions of the flow field for each inflow case, demonstrating that mode relevance depends on mode symmetry, turbulent kinetic energy content, and inflow characteristics. Cases with low turbulence intensity and large integral timescales show stronger correlations between POD modes and wake meandering, whereas higher turbulence conditions (turbulence intensity > 7%) are less effectively described by reduced-order models. However, the qualitative similarity of POD modes across varied atmospheric conditions suggests the potential existence of a semi-universal basis for representing wind turbine wakes, with implications for improving engineering wake models.

## 1. Introduction

Wake meandering, characterized by large-scale, quasiperiodic, low-frequency oscillations of the entire wind turbine wake, plays a crucial role in wind turbine loads, controller set point uncertainty, and power quality. Meandering significantly impacts power production [1] and fatigue loading [2] of downstream turbines in wind farms. Despite its importance, accurately representing wake meandering in numerical models remains challenging at any level of fidelity, making any additional characterization of the phenomenon valuable for improving wind farm performance and reliability.

Two prevailing hypotheses attempt to explain the origin of wake meandering. The externally driven hypothesis considers the wake's momentum deficit as a passive tracer advected by large-scale atmospheric turbulence [1]. This hypothesis suggests that turbulent structures larger than the rotor diameter contribute most significantly to wake meandering. This notion is further supported by España et al. [3], who demonstrated that large turbulence scales, particularly those in the atmospheric boundary layer, govern wake behavior. Baker and McGowan [4] and Zambrano et al. [5] also identified large-scale turbulence as a dominant factor in wake motion, with the former proposing a framework for turbulence-based wake modeling and the latter providing experimental data on wake turbulence dynamics.

In contrast, the internally driven hypothesis for wake meandering proposes that dynamic interactions between turbulent structures within the wake, such as tip vortices and hub/root vortices, generate pressure fluctuations substantial enough to displace the wake. Medici et al. [6] performed measurements on wake stability and internal vortical structures, while Okulov and colleagues [7] focused on the role of tip vortices in wake dynamics. Howard et al. [8] provided additional insight into the turbulence interactions within the wake that contribute to meandering. Foti et al. [9] explored the influence of shear instability on wake meandering, suggesting that such instabilities could be driven by both internal and external mechanisms. The internal mechanism for wake meandering has also been linked to shear instabilities by Andersen et al. [10] and Li et al. [11], both of whom investigated the onset of wake meandering as a function of environmental and turbine-specific factors. An alternative internally driven view attributes wake meandering to shear-instability waves in the wake shear layer. Andersen and Sørensen (2013) simulated shear-layer instabilities that excite meandering-like motions [10]. Li et al. (2022) numerically and theoretically identified critical shear parameters triggering wake oscillations [11].

Our ability to measure wind turbine wakes in the field has improved significantly over the past decade. More than ten years ago, some of the first dynamic wake measurements were collected by modifying a prototype lidar originally designed for vertical conical scanning [12]. These early measurements, despite their limitations, were used to validate basic assumptions of the dynamic wake meandering (DWM) model [13]. Today, lidar technology allows us to observe wake dynamics for wind turbines of any size, with the ability to scan spanwise and

* Corresponding author.
*E-mail address:* nicholas.hamilton@nrel.gov (N. Hamilton).

https://doi.org/10.1016/j.renene.2025.123555
Received 21 February 2025; Received in revised form 19 May 2025; Accepted 22 May 2025
Available online 10 June 2025

vertically in any direction, reach downstream distances on the order of kilometers, and capture wake meandering, the downstream trajectory of wake centers, expansion, and large-scale turbulent structures [14].

Nacelle-mounted lidars have emerged as a powerful tool for real-time characterization of inflow and wakes of utility-scale wind turbines [15]. Doppler lidars offer unique capabilities for wind energy research, including real-time measurements for turbine and farm control [16], high-resolution data assimilation [17] for numerical simulations, and detailed three-dimensional wake characterization [18]. Nacelle-mounted lidars specifically provide better characterization of the wind resource over the rotor span and remain aligned with the turbine's frame of references, which supports a wide range of advanced scientific and operational technologies, such as wake research and feed-forward controls [15].

Several recent studies leverage modern lidar technology to characterize turbulence in the wake. Depending on the instrument deployed, lidars typically measure in vertical planes at fixed downstream distances [19] or in horizontal planes perpendicular to the rotor at hub height [20]. These recent lidar-based studies have primarily looked at the temporal evolution of turbulence by identifying the wake within each scan and tracking its centerline position over time. The centerline is then used to quantify wake meandering for the sake of wake characterization [21] or model validation [22].

To investigate under what conditions we can expect the externally driven hypothesis to be the dominant mechanism driving wake meandering, we employ proper orthogonal decomposition (POD). This method is well-suited for identifying coherent turbulence structures in flow fields [23] and has been applied to wind energy for more than 15 years [24]. POD seeks the variance-maximizing structures that describe the turbulence in the flow, making it an ideal tool for quantifying potential meandering-inducing structures in the wake. If these structures are shown to contribute significantly to wake meandering, the reduced-order model (ROM) should reproduce the meandering behavior seen in the measurement data to a high level of fidelity [25]. Conversely, a ROM developed without these structures should fail to accurately reproduce wake meandering.

Through the use of POD, we estimate the meandering length scales and frequencies in our dataset and relate them to DWM modeling assumptions. The body of past experimental and numerical work typically characterizes the meandering frequency ($f_m$) in the context of a Strouhal number, $St = f_m D/U_{\text{hub}}$, defined in terms of the wind turbine rotor diameter ($D$) and hub-height inflow velocity ($U_{\text{hub}}$). Meandering frequencies are typically reported in the range of $0.1 \lesssim St \lesssim 0.35$, both in a laboratory setting [26,27] and field observations [14]. If the internally driven hypothesis for wake meandering is correct, the modes that contribute most to meandering should have characteristic frequencies higher than the inflow Strouhal number. Conversely, cases where the externally driven hypothesis is correct should favor structures with frequencies below the inflow Strouhal number.

DWM models typically consider only the inflow forcing, assuming the momentum deficit and wake center to advect as passive tracers carried by the background flow [28]. Typically, this effect is considered by applying a low-pass filter to the turbulent inflow such that only structures that exceed a certain minimum length scale influence wake motion. This cutoff length scale is often set to twice the observed instantaneous wake diameter, or simply as twice the rotor diameter ($2D$) in most implementations [29]. By combining advanced remote sensing measurements with statistical and applied mathematics analysis methods, we seek to develop an understanding of wake meandering across a wide range of atmospheric conditions. Ultimately, wake meandering can have large impacts on wind farm performance, so improved understanding of the underlying physics will contribute to the optimization of wind energy production and turbine longevity.

## 2. Methods

### 2.1. Wake meandering

Wake meandering is quantified in this work through the dynamics of the transverse coordinate of the wake center ($\mu$), which we estimate by fitting a Gaussian profile to the momentum deficit derived from the lidar scans. The velocity deficit is defined as

$$\tilde{u}(x, y, t) = 1 - \frac{u(x, y, t)}{U_{\text{hub}}(t)} \tag{1}$$

where $U_{\text{hub}}$ is the inflow hub-height velocity. In Eq. (1), $u$ represents the streamwise velocity measurement, estimated as the line-of-sight velocity observed by the lidar divided by the cosine of the beam angle [30], assuming perfect alignment between the nacelle and the bulk wind direction. Because our data are collected in approximately horizontal planes at hub height, we only consider lateral movements of the wake center along the $y$-direction at a fixed height above the ground, $z = z_{hub}$. The wake center is detected through a least-squares fit of a Gaussian function to the observed $\tilde{u}$ by the lidar at each downstream location and for each time:

$$\tilde{u}(x, y, t) = C_0 \exp \frac{1}{2} \left[ \frac{y - \mu(x, t)}{\sigma_w(x, t)} \right]^2 + C_1 \tag{2}$$

In Eq. (2), the peak momentum deficit is denoted as $C_0$, the standard deviation corresponding to wake width is $\sigma_w$, and the lateral wake center is $\mu$. An offset term, $C_1$, is included in the function, although it is typically a relatively small value, $-1 \lesssim C_1 \lesssim 1$ m/s.

### 2.2. Snapshot proper orthogonal decomposition

POD, also known as principal component analysis (PCA) or Karhunen–Loève decomposition, has been widely used in fluid dynamics for identifying coherent structures and reducing the dimensionality of complex flow fields [23]. However, its application to data in polar coordinates, as is more natural for scanning lidar observations, presents unique challenges that necessitate a careful reconsideration of the method's foundational elements.

Snapshot POD begins with a sequence of lidar observations, $\mathbf{X} = [\mathbf{x}_1, \ \ldots, \ \mathbf{x}_m]$, where each snapshot is a realization in the state space $\mathbf{x}_k \in \mathbb{R}^n$ at time $t_k$. POD seeks an orthonormal basis that optimally represents the data in terms of captured variance. When dealing with data in polar coordinates, the standard Euclidean inner product implicit in this formulation becomes inappropriate to adequately represent the distribution of turbulent kinetic energy (TKE) in the domain. The varying cell sizes in a polar grid lead to an inherent bias, overemphasizing contributions from larger radii. To address this, we modify the standard POD algorithm to incorporate a physically appropriate inner product for polar coordinates. Considering two snapshots $\mathbf{x}_l(r, \theta)$ and $\mathbf{x}_p(r, \theta)$, each of which represents the streamwise velocity (system state) vector in polar coordinates, we define a weighted inner product as

$$\langle \mathbf{x}_l, \mathbf{x}_p \rangle_W = \int_0^{2\pi} \int_0^R \mathbf{x}_l(r, \theta) \cdot \mathbf{x}_p(r, \theta)\, r \, dr \, d\theta \tag{3}$$

For discrete data on a polar grid with spacing $\Delta r$ and $\Delta\theta$ in the radial and azimuthal directions, respectively, Eq. (3) becomes

$$\langle \mathbf{x}_l, \mathbf{x}_p \rangle_W = \sum_{i=1}^{N_r} \sum_{j=1}^{N_\theta} \mathbf{x}_l(r_i, \theta_j) \cdot \mathbf{x}_p(r_i, \theta_j)\, r_i \, \Delta r \, \Delta\theta \tag{4}$$

By recasting the observations $\mathbf{X}$ as the vector $[\mathbf{x}_l(r_1, \theta_1), \ldots, \mathbf{x}_l(r_1, \theta_{N_\theta}), \ldots, \mathbf{x}_l(r_{N_r}, \theta_1), \ldots, \mathbf{x}_l(r_{N_r}, \theta_{N_\theta})]$ for $l \in [0, N_m]$, the inner product in Eq. (4) can be conveniently represented by a diagonal weight matrix $\mathbf{W}$:

$$\mathbf{W} = \text{diag}(r_1, \ldots, r_1, r_2, \ldots, r_2, r_3, \ldots, r_{N_r}, \ldots, r_{N_r}) \Delta r \Delta\theta \tag{5}$$

where each radial coordinate, $r_i$, is repeated $N_\theta$ times.

The new inner product is incorporated into the POD algorithm by modifying the correlation matrix to account for the weights described by Eq. (5) as

$$\mathbf{C} = \frac{1}{m}\mathbf{X}^{\intercal}\mathbf{W}\mathbf{X} \tag{6}$$

The POD modes are then obtained by solving the eigenvalue problem in the standard fashion:

$$\mathbf{C}\mathbf{v}_i = \lambda_i \mathbf{v}_i \tag{7}$$

where $\lambda_i$ are the eigenvalues and $\mathbf{v}_i$ are the corresponding eigenvectors. The POD modes $\boldsymbol{\phi}_i$ are then reconstructed as

$$\boldsymbol{\phi}_i = \frac{1}{\sqrt{\lambda_i}}\mathbf{X}\mathbf{v}_i \tag{8}$$

This formulation ensures that the POD modes accurately reflect the true spatial scales and TKE of the flow structures in polar coordinates, without bias toward structures at larger radii. A set of projection coefficients, $a_i$, describe the amplitude of each mode in time and are sought by projecting the observational data $\mathbf{X}$ onto the collection of POD modes $\boldsymbol{\Phi}$ and integrating over the domain, $\Omega$, as

$$\mathbf{A} = \int_{\Omega} \mathbf{X}^{\intercal}\boldsymbol{\Phi}\, d\Omega \tag{9}$$

Mode projection coefficients are described by the column space of $\mathbf{A} = [a_0, a_1, \ldots, a_N]$.

This adaptation of the standard snapshot POD algorithm maintains the core principles of POD while adapting it to the geometric constraints of polar coordinate systems, aligning with the theoretical perspective that the choice of inner product in modal decompositions should reflect the physics of the problem at hand [31]. By incorporating an inner product motivated by the polar description of the state vector, we extend the applicability of POD to the natural coordinate system of scanning Doppler lidars and open the method to a wider class of atmospheric science and wind energy problems.

### 2.3. Reconstruction

The approach to velocity field reconstruction used in this work relies on the nature of the POD to organize input system dynamics into coherent structures. We develop a combinatorial approach to reduced order modeling to identify the turbulent structures (POD modes, $\phi_i$) that contribute most to wake meandering. Each combination of modes was determined by selecting $k$ of the first $N_m = 14$ modes, where $k \in [3, \ldots, 14]$. The maximum number of modes, $N_m$, corresponds to a threshold of 90% of the TKE represented in the observational basis for each observed case. Flow fields reconstructed with each unique combination of modes are then used to estimate wake meandering identically as for the lidar scans, as described in Section 2.1.

In each of the ROMs, the zeroth mode, $\phi_0$, representing the momentum deficit of the wake, is also included. The total number of combinations for each dataset was $K = \sum_{k=3}^{14}\binom{N_m}{k} = 16{,}278$. Fig. 1 shows the number of combinations tested for each value of $k$. For each ROM, velocity fields are reconstructed from the truncated basis, summing over selected mode indices rather than a sequential set up to a maximum. For each combination, $I$, the reconstructed velocity field is

$$\hat{u}(\boldsymbol{x}, t) = \sum_{i \in I} a_i(t)\boldsymbol{\Phi}^{(i)}(\boldsymbol{x}) \tag{10}$$

where the index $i$ may take only the values included in a particular combination of modes and the hat notation indicates a low-dimensional representation of the velocity field. In Eq. (10), the velocity field and modal basis have been denoted as scalars, as only the streamwise component of velocity is considered.

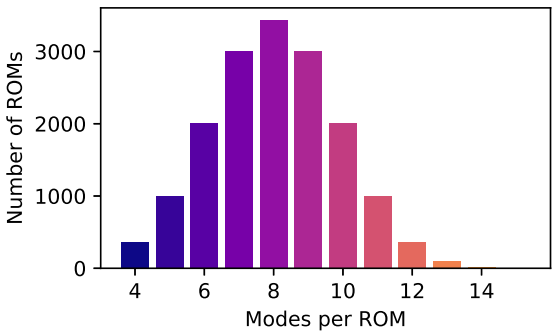


**Fig. 1.** The number of mode combinations used to reconstruct the flow field for a given maximum number of modes considered ($k$).

## 3. Data

This study uses nacelle-mounted scanning lidar data and atmospheric inflow measurements from two recent DOE-funded field campaigns: the American WAKE ExperimeNt (AWAKEN) [32] and Rotor Aerodynamics, Aeroelastics, and Wake (RAAW) [33] projects.

AWAKEN is a multi-institutional campaign that gathers data on wind farm-atmosphere interactions, which contribute to uncertainty in wind plant performance models. Atmospheric conditions were characterized using data from a surface flux station [34] and a meteorological tower [35] at site A1 (see Fig. 2). The surface flux station, equipped with a Gill R3-50 sonic anemometer mounted on a 4-m tripod, recorded data continuously at 20 Hz. Data acquisition software, originally developed by Argonne National Laboratory for the ARM ECOR system in 2003, was adapted for AWAKEN to work with the Gill Sonic R3 series anemometers [36]. Sensible heat flux and momentum flux were processed into 30-minute-resolution data, assuming a constant relative humidity of 50% due to the absence of real-time humidity measurements. Hub-height wind speed and direction were recorded with a Thies 3D ultrasonic anemometer. Turbulence intensity was calculated as the standard deviation of wind speed divided by the mean wind speed over a 10 min period. Wind directions were limited to 170° to 200°, corresponding to the peak of the wind rose in Fig. 2, which also restricted times when the wake from a neighboring turbine was visible.

The RAAW project studies the response of a modern flexible rotor to the turbulent atmospheric inflow [33]. Atmospheric inflow conditions for the RAAW data cases are derived from a 183.5-m guyed meteorological tower [37], instrumented with five cup anemometers, three ultrasonic anemometers, three vanes, three barometric and temperature sensors, and one humidity sensor. Ultrasonic anemometers reported data at 20 Hz, and all other instruments reported data at 1 Hz. Near-surface measurements of momentum and heat flux were provided by a surface met station [37], deployed 10 m southwest of the meteorological tower. This station hosted an ultrasonic anemometer 2.5 m above ground and probes for atmospheric pressure, temperature, and humidity 2 m above ground. As with the tall tower sensors, the anemometer reported data at 20 Hz, and the other sensors reported data at 1 Hz. Fig. 3 shows the experimental arrangement of the RAAW project, including the met tower, surface met station, and turbine. Additional details for measurements are provided in Table 1.

Both the RAAW and AWAKEN projects feature GE 2.8-MW turbines with 127-m rotor diameters. The RAAW project used a prototype R&D turbine in Lubbock, Texas, with a hub height of 120 m, while AWAKEN used production-run GE 2.8–127 turbines with a hub height of 88.5 m. Both projects employed Halo Photonics Streamline XR+ Doppler scanning lidars positioned on the aft sections of the nacelles (for the AWAKEN [38] and RAAW [39] projects). These were configured for various measurement strategies, including plan-position indicator (PPI) scans to measure fluctuating wake flow fields.

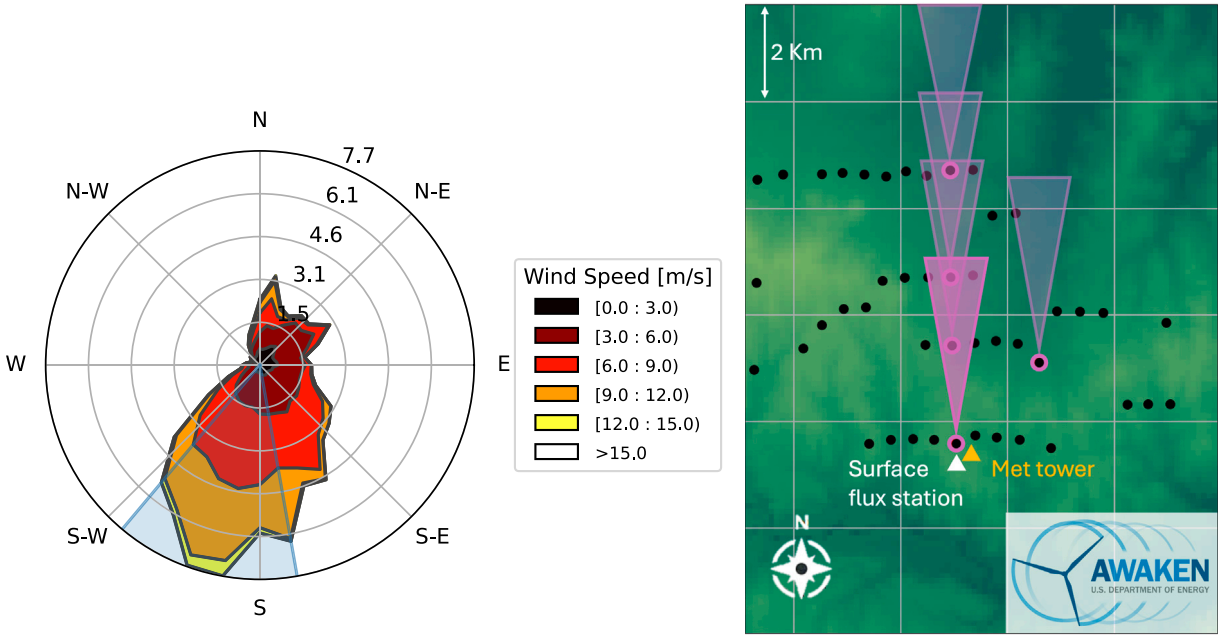


**Fig. 2.** Wind rose showing selected wind direction sector in blue (left) and high-level schematic (right) of the AWAKEN project.

**Table 1**
Description of lidar, met tower, and surface met station datasets for AWAKEN and RAAW experiments.

| | AWAKEN | RAAW |
|---|---|---|
| Number of cases | 54 | 11 |
| | Lidar | |
| Lidar type | Halo streamline XR+ | Halo streamline XR |
| Scan duration | 10 s | 18 s |
| Azimuth limits | −15°–15° | −15°–15° |
| Azimuthal resolution | 1.5° | 2° |
| Range limits | 105–2265 | 105–2265 |
| Range gate length | 30.0 m | 12.0 m |
| Number of scans | 160–175 | 45–50 |
| Upsampled scans | 1650–1700 | 680–725 |
| Upsampled resolution | 1 s | 1 s |
| | Met tower (Hub height) | |
| Wind speed | Windsensor P2546D | Thies clima first class anemometer |
| Sampling frequency | 1 Hz | 20 Hz |
| Wind direction | Thies FC vane | MetOne wind vane |
| Sampling frequency | 1 Hz | 20 Hz |
| | Surface met station | |
| Resolution | 30 min | 10 min |
| Derived quantities | Sensible heat flux (W/m$^2$) | Kinematic heat flux (m/s K) |
| | Momentum flux (kg/m s$^2$) | Kinematic momentum flux (m$^2$/s$^2$) |
| | Friction velocity (m/s) | Friction velocity (m/s) |
| | Monin–Obukhov length (m) | Monin–Obukhov length (m) |

Wake PPIs were designed using the LiSBOA tool [40], sweeping approximately 1.2° of azimuth per second, covering a sector of approximately 30° centered downstream of the turbine. Lidar data were quality controlled using the Field EXperiments Tool Arsenal (FIEXTA) software [41], which implements dynamic filtering methods [42]. Data were temporally upsampled using local advection velocities and the time delays between successive beams at similar azimuth angles [43], producing line-of-sight velocity 'snapshots' at a temporal resolution of 1 s.

While the lidars are capable of making measurements up to 4 km from the wind turbine, the measurement quality in the far range is typically quite low, and wakes are often fully recovered far sooner. Additionally, the data collected in the AWAKEN project include only inflows from a southerly sector, and the downstream row of turbines is often visible in the scan data. To preclude observations of wakes of neighboring turbines from influencing wake center estimates, which would complicate the modal analysis undertaken below, scans are constrained to ranges where $2.5 \leq x/D \leq 10$ and azimuth angles $-15° \leq \alpha \leq 15°$.

Scanning lidar provides line-of-sight wind speed, $v_{los}$, which is transformed into the streamwise velocity based on

$$v_{\text{los}} = u_{\text{hor}}(r, \alpha, t)\cos(\zeta)\cos(\alpha - \theta) + w(r, \alpha, t)\sin(\zeta) \tag{11}$$

where $u_{\text{hor}}$ is the horizontal wind speed, $r$ is the range along the laser beam, $\zeta$ and $\alpha$ are the elevation and azimuth angles, respectively (measured from $x_{\text{lidar}}$, $t$ is time, and $\theta$ is the wind direction (see Fig. 4). For all lidar measurements used in this analysis, the elevation angle was fixed at $\zeta = 0°$, simplifying the relationship between $v_{\text{los}}$ and $u_{\text{hor}}$. Also, by assuming negligible yaw error of the turbine, that is $\theta \sim 0$ in

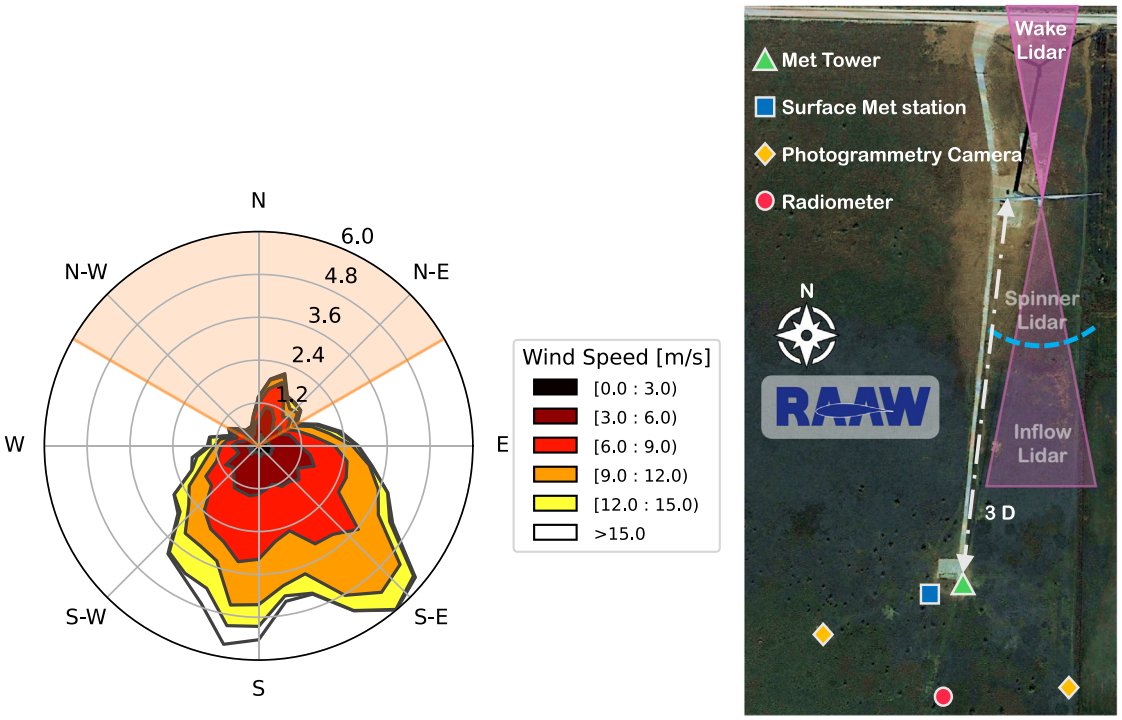


**Fig. 3.** Wind rose showing excluded wind direction sector in orange (left) and high-level schematic (right) of the RAAW project.

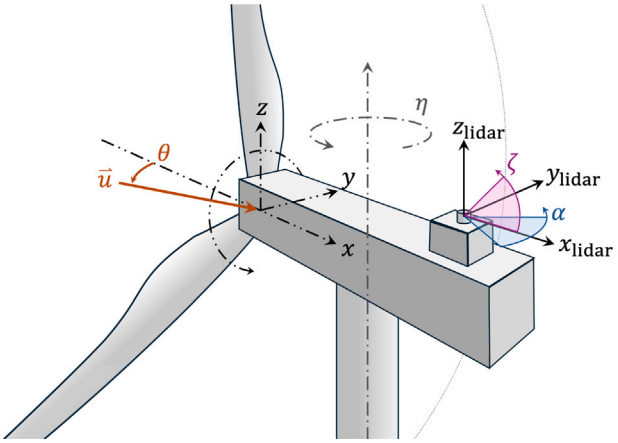


**Fig. 4.** Schematic relating the reference frame of the nacelle-mounted scanning lidar to the wind turbine and the inflow, $\vec{u}$.

the lidar frame of reference, yields the compact expression:

$$u(r,\alpha,t) \sim u_{\mathrm{h}}(r,\alpha,t) \sim \frac{v_{\mathrm{los}}(r,\alpha,t)}{\cos\alpha}, \tag{12}$$

where $u$ is the instantaneous local streamwise velocity. This formulation assumes perfect alignment of the turbine with the flow, $\theta \sim 0$, which is reasonable in a spatially and temporally averaged sense, as the rotor slowly reacts to bulk changes in wind direction [44]. However, through Eq. (12) we enforce alignment in a local and instantaneous sense to the turbulent field. This is equivalent to neglecting the instantaneous local transversal velocity component [30]. This is a common approach when dealing with turbulence analysis from a monostatic lidar [45] and is expected to minimally affect the estimation the wake center.

Measurement cases combining lidar datasets and inflow measurements were considered only after passing through the following quality control filters. Each filter is followed by a metric indicating the portion of the population of data that were disallowed and a description. Note that more than one filter condition was applicable to many of the data points.

**Sensor Quality—6%** Measurement cases combining lidar datasets and inflow measurements were considered only after filtering out stuck, broken, or defective sensors. This ensures that all required measurements are reliable and eliminates cases where data are missing or sensors fail to report reasonable observations.

**Wind Direction Sector—34%** Cases were filtered to include only wind directions within the appropriate sector. This is crucial because we rely on the characteristics of the inflow to contextualize wind turbine wake meandering. For the AWAKEN project, this step also ensures that only the wake dynamics from the single turbine of interest are present in the lidar scans.

**Yaw Travel Limitation—51%** Only cases with a total yaw travel below 20° were considered. In both the RAAW and AWAKEN projects, the wind turbine operates at a nominal control point, allowing the rotor to yaw and optimally align with the incoming wind. Yaw activity is evident in lidar scans as abrupt changes or sweeping movements of the wakes within the scanned sectors. Very few lidar scan periods are completely free from yaw activity, hence the 20° travel limitation.

**Power Production Threshold—18%** Cases were filtered to include only those where active power is greater than 150 kW and that power generation is within one standard deviation of the nominal power curve. This criterion ensures that the turbine is operating nominally and that a wake will be evident in the lidar data. The selection allows for describing wake meandering under a wide range of atmospheric conditions and inflow wind speeds.

**Variability Filtering—10%** As a final quality control step, cases were excluded where the total variation exceeded the 90th percentile. Following the method outlined by Hamilton [46], total variation is defined as the determinant of the covariance matrix relating

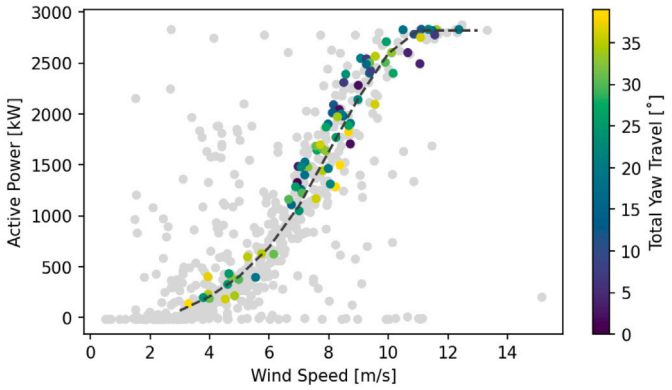


**Fig. 5.** Power curve from turbine H05 at the King Plains Wind Plant. All available cases are shown with gray points, cases selected for analysis in the current work are colored by the total yaw travel of the turbine during the measurement period. The nominal power curve (black dashed line) was calculated from an open-source model [47].

inflow wind speed, wind direction, turbulence intensity, turbine power production, and nacelle position signals from the SCADA record. This step ensures that only statistically stationary conditions are considered, eliminating cases with drastically changing atmospheric conditions or significant turbine control actions during the lidar scan period.

A total of 65 cases were retained after applying each of the quality control filters enumerated above, including 54 cases from the AWAKEN project and 11 cases from the RAAW project. Fig. 5 shows the distribution of the full range of cases with wake PPI scans. Cases that did not pass all of the quality control measures listed above are shown in gray. The final cases selected for analysis are highlighted in the figure according to the total yaw travel observed during the respective wake scanning period.

## 4. Results

The integral timescale of atmospheric turbulence provides a measure of the temporal correlation of velocity fluctuations in the atmospheric boundary layer. The autocorrelation coefficient $\rho(\tau)$ is then defined as

$$\rho(\tau) = \frac{\langle u'(t)u'(t+\tau)\rangle}{\sigma^2} \tag{13}$$

where $u'(t)$ represents the turbulent velocity fluctuations, $\tau$ is the time lag, $\langle\cdot\rangle$ denotes the ensemble average, and $\sigma^2$ is the variance of the velocity fluctuations. The integral timescale $T$ is calculated by integrating the autocorrelation function up to the point where it decays to a specified threshold:

$$T = \int_0^{\tau_c} \rho(\tau), d\tau \tag{14}$$

Here, $\tau_c$ represents the correlation decay limit, typically chosen as the point where $\rho(\tau) = 0.05$, rather than the first zero-crossing point to account for sampling errors [48]. This integration captures the temporal coherence of turbulent fluctuations, providing insight into the characteristic timescales of atmospheric turbulence. In practice, this calculation was performed using 20-Hz wind speed measurements from a sonic anemometer positioned at hub height for the turbines in each project, with computations based on 30 min averaging periods.

Fig. 6 shows the distribution of inflow wind speed, $U_\infty$, integral timescale, $T$, and inflow Strouhal number, $St_{\text{in}}$ for each of the 65 cases from the combined RAAW and AWAKEN experiments. The integral timescales, $T$, are taken as the characteristic period of the fluctuation in the velocity field and are used to define the characteristic frequency of turbulent fluctuations in the discussion of meandering frequencies.

Average scans for selected cases are shown in Fig. 7 and highlight differences in the peak momentum deficit and recovery rate of wakes in different atmospheric conditions. While all datasets include some yaw activity, the average wake is centered around $\alpha = 0$. Each of the time-averaged velocity fields in Fig. 7 highlights characteristics of the wind turbine wake as well as the influence of the atmospheric forcing conditions and effects of the wind turbine operations and controls. The data quality control preferentially selects the most statistically stationary cases from the full population of data. As a consequence, there is a bias toward stable atmospheric conditions in which the yaw travel was minimized during the lidar collection periods of both experiments.

Yaw activity is not directly evident in the time-averaged wakes. However, Fig. 8 shows a time-azimuth cross section of a single dataset at a range of approximately $x/D = 8$ (1 km), in which the wake is highlighted as a low wind speed region that persists in time across the figure. Meander in the azimuthal direction seen in the figure combines the effects of several factors. While the wake center does travel horizontally, there are also translations of the wake center introduced by the yaw activity of the rotor. Horizontal wake center locations, $\mu$, are estimated as the center location of the Gaussian function fit to the velocity deficit, as in Eq. (2). Yaw activity becomes especially evident in the time histories of detected wake centers, presented in Fig. 9. Yaw activity, illustrated by the dashed black line and related vertical axis on the right, are evident in the detected centers as sudden shifts in the wake center time histories. Because changes in the nacelle position impact the apparent wake centers uniformly at all ranges, a simple correction can be applied to the wake centers as $\Delta\mu = r\sin\alpha$, where $r$ indicates the distance from the lidar (range), and $\alpha$ indicates the nacelle orientation with respect to the position at the beginning of each dataset. Correcting for changes in nacelle position throughout each dataset is important to correctly characterize the distributions of wake centers and their dynamics in the turbine frame of reference. It should be noted that turbines take yaw-correcting actions only after an integrator of error between the measured wind direction and the nacelle position exceeds a threshold. This means that in most cases there remains some influence of yaw misalignment on the detected wake centers, even after correcting for yaw activity. Without a time history, it is not possible to accurately account for the yaw error. However, this sort of misalignment is part of the nominal operation of a turbine under normal control conditions and is a possible trigger for wake meandering.

An example of the momentum deficit measured by the lidar is shown in Fig. 10 in blue, along with local fits of the Gaussian function in black and detected wake centers as red points. Each of the subfigures indicate a good level of agreement between the momentum deficit and fit function, building confidence in the Gaussian model of the wake. Alternative methods of detecting the wake centers have been explored in the literature,[14] including a momentum-centroid approach and local minimum velocity methods, but are not explored in the current work for brevity.

An alternative view of the detected wake centers is provided in Fig. 11, where $\mu/D$ is noted on the lidar scans as points colored by their respective $R^2$ values. In both examples, it is evident that the $\mu/D$ follows the bulk momentum deficit in the wake quite closely. A bias of $\mu/D$ toward positive values of $y/D$ in the near wake $x/D \lesssim 3$ is also visible in the scan taken at 2023-09-04 10:42:15 UTC (left). This bias, which persists throughout many of the scans, arises from the asymmetric double-Gaussian profile of the momentum deficit very near the turbine, described in analytical models in [49,50]. Positive bias of $\mu/D$ in the near wake is not easily corrected, and leads to impacts later in the analysis, including power spectral densities an representation with the ROMs.

Wake meandering combines the downstream advection of $\mu$ by the mean flow and turbulent structures in the wake. Trajectories of $\mu$ throughout the measurement domain are shown in Fig. 12 (left)

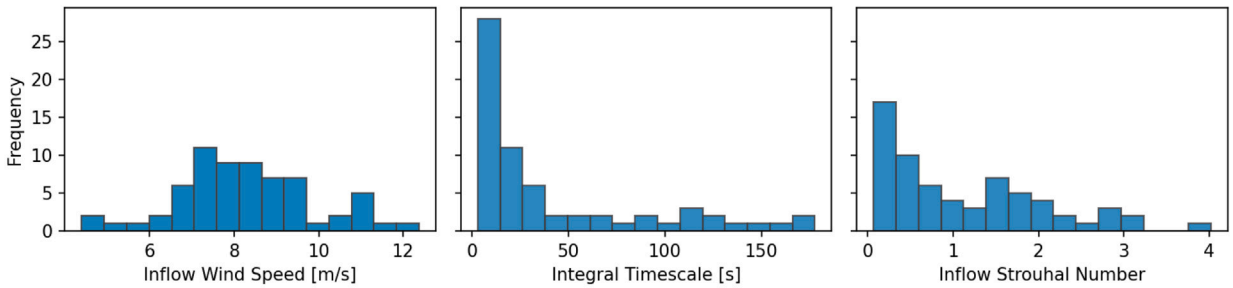


**Fig. 6.** Distributions of the average inflow wind speed, $U_\infty$, integral timescale, $T$, and Strouhal Number, $St_{\text{in}}$, at hub height for the subset of conditions corresponding to the 65 selected cases.

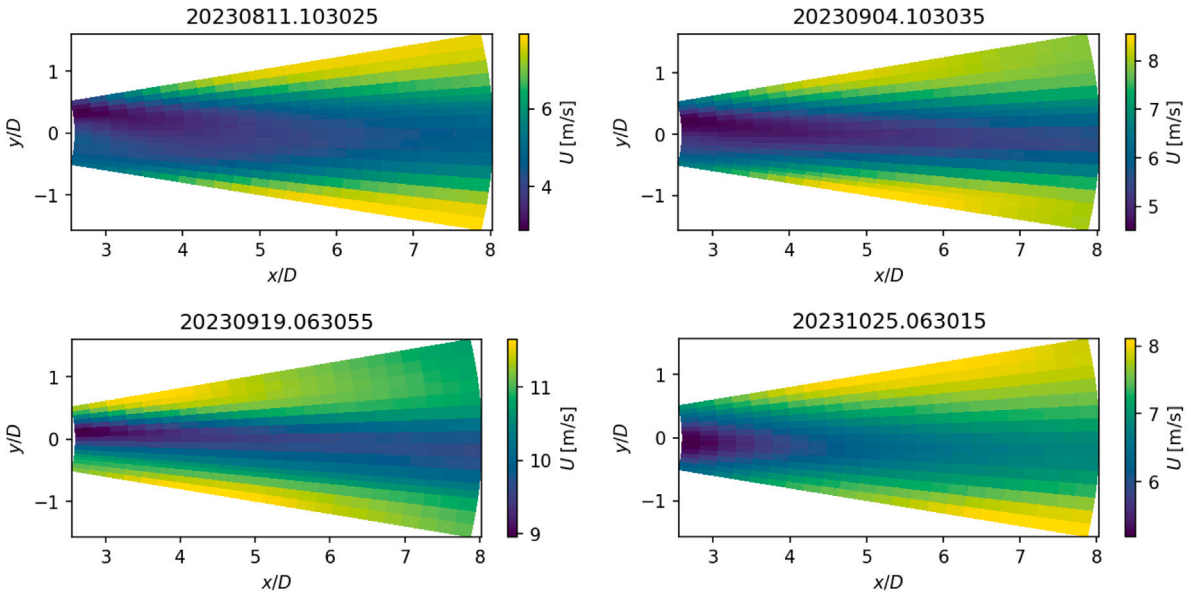


**Fig. 7.** Average wake velocity fields for 2023-08-11 10:30 (top left), 2023-09-04 10:30 (top right), 2023-09-19 06:30 (bottom left), 2023-10-25 06:30 (bottom right) showing a range of background velocities, momentum deficits, and wake recovery rates.

for several times in the dataset. The meander is also evident in the trajectories as a local tendency back toward positive values of $y$. The amplitudes of these meandering structures also tend to increase as they advect downstream. Kernel density estimates of wake center locations are shown in Fig. 12 (right), highlighting the tendency of the $\mu$ to spread out at greater streamwise distances.

In addition to statistical descriptions of the wake center, we are also interested in dynamics of wake meandering, specifically relating the characteristic frequencies of wake meandering, quantified through power spectral densities (PSD, Eq. (15)) to inflow conditions and the POD modes, $\phi_i$. PSDs are calculated using Welch's method as

$$S_{\mu\mu}(f) = \frac{1}{L}\sum_{k=1}^{K}\frac{1}{N}\left|\sum_{n=1}^{N}\mu_k(n)e^{-i2\pi fn/N}\right|^2 \tag{15}$$

where $K$ is the number of segments, $L = 512$ samples is the number of points in the fast Fourier transform, $N = 1024$ is the length of each segment, and $\mu_k(n)$ is the $k$th segment of the time series. A uniform window function is applied to each segment in the calculation of the PSDs. The reduced frequency, $f_s = fD/U_\infty$, is normalized by considering the average inflow velocity recorded by the met towers, $U_\infty$, and the turbine's rotor diameter, $D$.

Fig. 13 (left) shows $S_{\mu\mu}$ as a function of the reduced frequency at several downstream distances in the wake. The pink vertical line indicates the inflow Strouhal number, $St_{in}$, which acts as the cutoff frequency for wake meandering in the remainder of the results. Fig. 13 (right) shows the premultiplied spectra $f_s^{5/3}\cdot S_{\mu\mu}$, which highlights the deviation of the meandering spectra from the classical turbulence decay law. The meandering frequency is defined as the reduced frequency at which the maximum value of the premultiplied spectrum occurs:

$$f_m = \text{argmax}\ f_s^{5/3}\cdot S_{\mu\mu}(f_s) \tag{16}$$

The normalized amplitude of wake meandering is assessed considering the PSD of $\mu$ at $f_m$, $A_m = \sqrt{S_{\mu\mu}(f_m)}$. Fig. 14 compares the meandering amplitudes and frequencies for each of the 65 cases considered in this study, colored by the inflow velocity. As a general observation, the range of meandering frequencies shown in the combined AWAKEN and RAAW datasets is $0.1 \le f_m \le 0.7$, which is slightly larger than the range reported in past studies.

The snapshot POD introduced in Section 2.2 requires state space observations with consistent dimensions and coordinates, making it impractical to correct for yaw before decomposition. Remapping wake observations from lidar scans onto a corrected reference frame downstream of the turbine would introduce inconsistencies in the azimuthal coordinates or create empty radial slices, both of which would complicate the eigenvalue decomposition central to the POD analysis.

Each of the 65 cases has azimuth coordinates that vary slightly due to the continuous scan operation of the lidar, which assigns nominal azimuth angles after a set time delta. Operational delays, data transmission, and status checks cause small variations in the number of scans per dataset. This analysis focuses on the low-rank POD modes that account for most of the TKE in the lidar scans. Although the energy

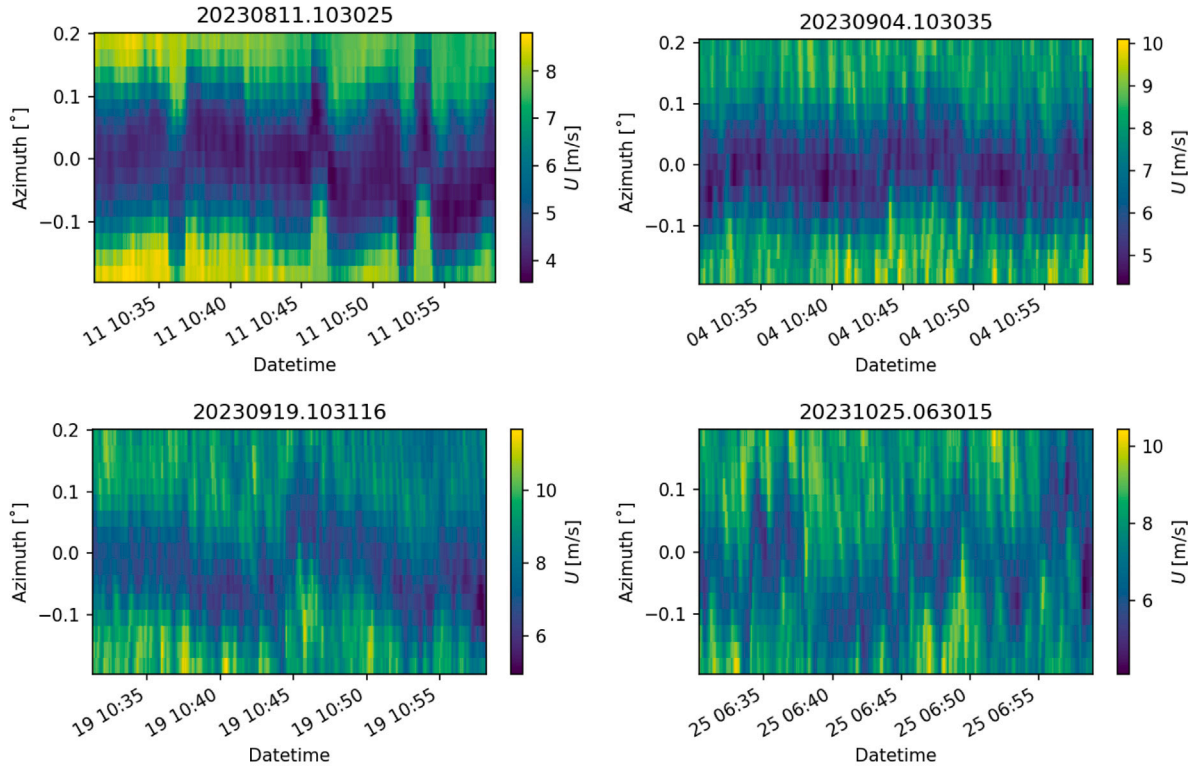


**Fig. 8.** Wake velocity at a fixed downstream distance of $x/D = 8$ for observations at 2023-08-11 10:30 UTC (top left), 2023-09-04 10:30 UTC (top right), 2023-09-19 06:30 UTC (bottom left), 2023-10-25 06:30 UTC (bottom right).

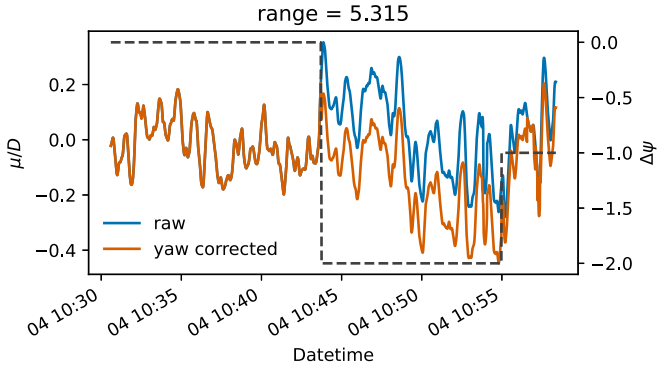


**Fig. 9.** Detected wake centers directly from lidar observations (blue) and after correcting for yaw activity of the turbine (orange). The dashed black line indicates nacelle position changes from the beginning of the time series and corresponds with the axis labels on the right.

distribution across POD modes varies between datasets, researchers order the modes by descending energy, with the eigenvalue $\lambda_i$ of each mode representing the energy distribution.

We use only the first 14 POD modes, which capture the most coherent structures in the lidar scans, to reconstruct flow fields for meandering analysis. The eigenvalues $\lambda_i$ quantify the TKE captured in each reduced-order model (ROM), directly measuring reconstruction error. Missing energy in a ROM remains bounded by the smallest mode eigenvalue included in the reconstruction. Fig. 15 illustrates the distribution of TKE described by the POD modes across all cases. This analysis excludes the energy of the zeroth mode $\phi_0$, which represents the mean flow field, ensuring the normalized sum represents only the TKE. The black dashed line in the figure identifies the threshold at which the POD modes capture 90% of the TKE. In some cases, as few as four modes meet this threshold, while other cases require more modes. In all but two outlier cases, the POD meets the 90% TKE threshold with a maximum of 14 modes.

We apply the POD independently to each lidar dataset, producing a unique basis of modes for each case. Fig. 16 shows the POD modes associated with the case beginning at 2023-09-04 10:30 UTC. Although the mode bases differ quantitatively for each case, their structure and order remain qualitatively similar. Colorbars are included with each mode for completeness, although the units and quantitative values only become meaningful when they combine the modes with their respective coefficients to form a ROM.

The zeroth mode, $\phi_0$, represents the mean flow, capturing the characteristic momentum deficit in the wind turbine wake (see Table 2). It should be noted here that the basis of observations comprises the instantaneous velocity, rather than just the fluctuations. Thus, the zeroth mode is a true POD mode with a time-varying coefficient and represents dynamics of the momentum deficit. Modes $\phi_1$ through $\phi_{14}$ describe coherent wake structures ranked by their contributions to the lidar scans. The first mode, $\phi_1$, accounts for 20% to 80% of the TKE and primarily describes lateral shifts in the wake, crucial for wake meandering. Mode $\phi_2$ represents a full oscillation in the streamwise ($x$) direction and a half oscillation in the transverse ($y$) direction, reflecting large streamwise wake variations. Mode $\phi_3$ introduces an additional half-period in $x$, describing 1.5 periods in the lidar scan domain.

Higher-order modes become increasingly complex and difficult to assign a concise description. Mode $\phi_4$ exhibits significant azimuthal asymmetry, complicating direct interpretation. In contrast, $\phi_5$ is symmetric, describing a full oscillation in $x$ and possibly reflecting vertical wake meandering. Mode $\phi_9$ describes two full periods in $x$, further illustrating the complexity of higher-order structures. Azimuthal symmetry is defined here as a cosine distance, $d$, between the upper ($y+$) and lower ($y-$) halves of the PPI scan sector across the time-averaged wake center, nominally at $y/D = 0$, and is posed mathematically as

$$\kappa(\phi_i) = \frac{\phi_{i,y+} \cdot \phi_{i,y-}}{\|\phi_{i,y+}\| \|\phi_{i,y-}\|} \tag{17}$$

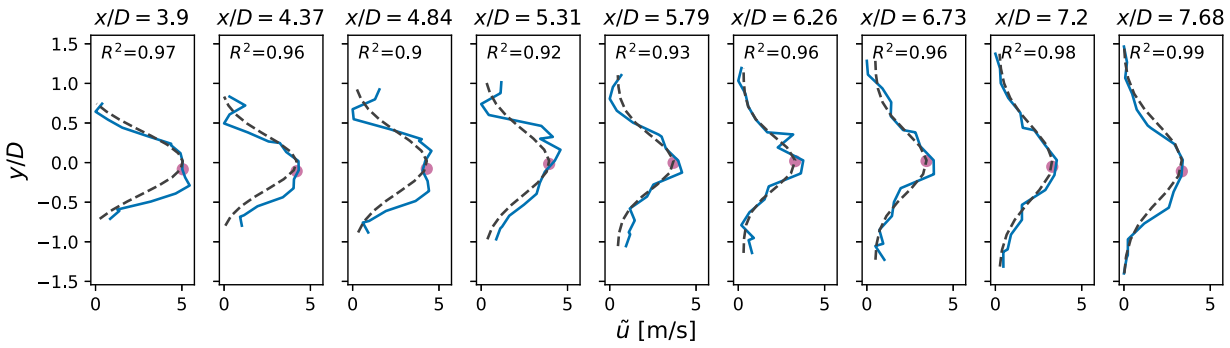


**Fig. 10.** Detected wake centers showing Gaussian fit against momentum deficit. Blue lines indicate momentum deficit estimated from lidar scans, dashed line shows the fit Gaussian profile, point marker is the detected wake center $\mu/D$.

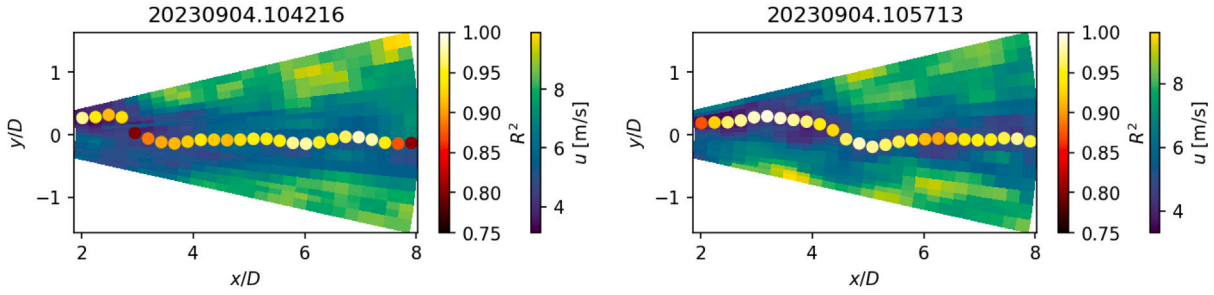


**Fig. 11.** Example lidar scans showing $u$ overlaid with the fitted wake centers. Detected wake centers are colored by their respective coefficient of determination.

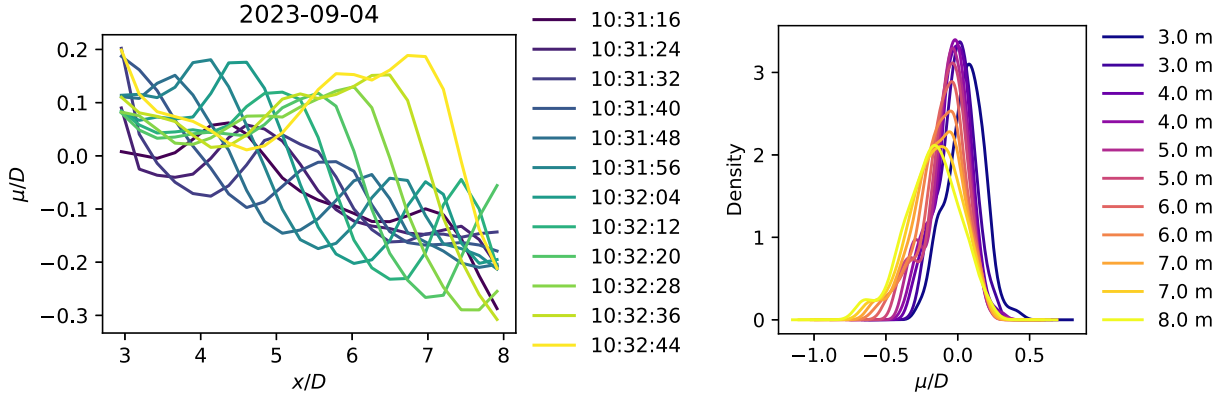


**Fig. 12.** Wake center trajectories for selected times (left) and kernel density estimates of wake centers by distance downstream of the lidar (right).

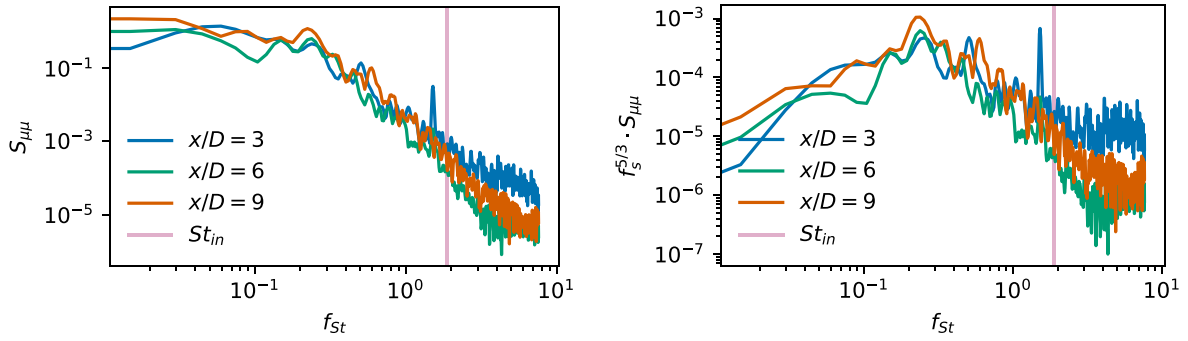


**Fig. 13.** Power spectral densities (left) and premultiplied spectra (right) of detected wake centers from the lidar data at selected downstream distances.

By nature of the cosine distance, modes that are perfectly symmetric show behavior where $\phi_{i,y+} = \phi_{i,y-}$, which leads to a cosine distance of $\kappa(\phi_i) = 1$. Similarly, antisymmetric modes are those for which $\phi_{i,y+} = -\phi_{i,y-}$, leading to $\kappa(\phi_i) = -1$. Modes characterized as asymmetric in the current study are those for which $|\kappa(\phi_i)| \leq 0.3$. The cosine distance for each mode shown in Fig. 16 is shown in Table 2.

**Table 2**
Description of POD mode structure, periodicity, and associated eigenvalue.

| Mode, $i$ | Structure | $\kappa(\phi_i)$ | Description |
|---|---|---|---|
| 0 | symmetric | 1.00 | Mean momentum deficit of the wake |
| 1 | antisymmetric | −0.94 | Full period in $y$, half-period in $x$ |
| 2 | antisymmetric | −0.78 | Contains a full period each in $x$ and $y$ |
| 3 | antisymmetric | −0.81 | Represents 1.5 periods in $x$ and one period in $y$ |
| 4 | asymmetric | −0.30 | Significant azimuthal and radial asymmetry |
| 5 | symmetric | 0.65 | Describes 1 full period in $x$ |
| 6 | symmetric | 0.39 | 1.5 periods in $x$ |
| 7 | asymmetric | −0.18 | Highlights shear layer at negative $y$ |
| 8 | symmetric | 0.48 | May represent 1.5 periods each in $x$ and $y$ |
| 9 | symmetric | 0.48 | Describes 2 full periods in $x$ |
| 10 | asymmetric | −0.21 | Phase-offset, but similar to $phi_7$ |
| 11 | symmetric | 0.40 | Highlights shear layer at positive $y$ |
| 12 | asymmetric | 0.02 | Shows 2.5 periods in $x$, 2 periods in $y$ |
| 13 | symmetric | 0.34 | Phase-offset, but similar to $phi_{12}$ |
| 14 | asymmetric | −0.13 | Higher order, but similar to $phi_7$ |

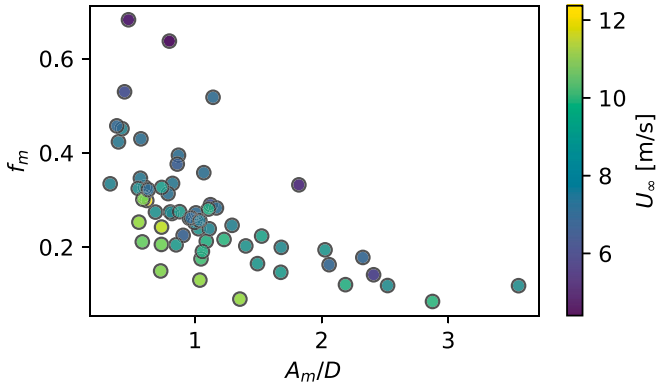


**Fig. 14.** Relationship between meandering amplitude, frequency, and inflow velocity.

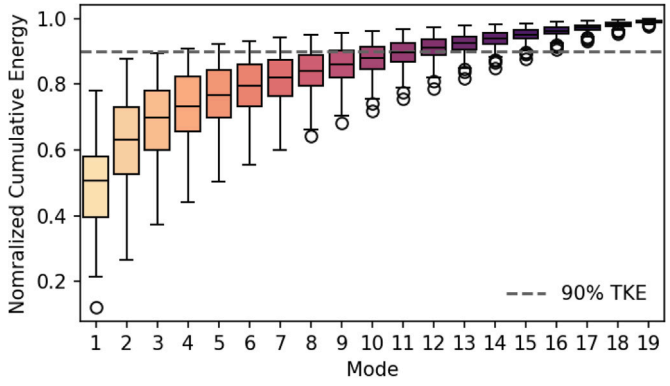


**Fig. 15.** The distribution of cumulative TKE described by the POD eigenvalues for the collection of 65 cases.

Following Eq. (10), we reconstruct the flow field using 16,278 unique subsets, including 3–14 POD modes in addition to $\phi_0$ representing the momentum deficit of the wake. Fig. 17 shows the combinations, ranging from ROMs with only three turbulent modes and $\phi_0$ on the right, to those incorporating more modes on the right. Each reconstructed wake profile was fitted to a Gaussian function (Eq. (2)) to estimate the lateral wake center, $\hat{\mu}$.

When reconstructing velocity fields using POD modes, we aim to match the PSD of wake center locations from the reconstructed field, $S_{\hat{\mu}\hat{\mu}}$, to the original field, $S_{\mu\mu}$. We consider mode combinations that reproduce wake meandering (i.e., $S_{\mu\mu} \approx S_{\hat{\mu}\hat{\mu}}$) representative of wake meandering in the low-order velocity field. Coherence, defined in Eq. (18), quantifies the similarity between wake center trajectories in the lidar scans and ROMs:

$$C_{\mu\hat{\mu}}(f,x) = \frac{|S_{\mu\hat{\mu}}(f,x)|^2}{S_{\mu\mu}(f,x)S_{\hat{\mu}\hat{\mu}}(f,x)} \tag{18}$$

Here, coherence $C_{\mu\hat{\mu}}(f,x)$ measures the similarity of wake center dynamics at frequency $f$. A value of $C_{\mu\hat{\mu}}(f,x) = 1$ indicates a perfect match between PSDs, while $C_{\mu\hat{\mu}}(f,x) = 0$ indicates no match.

PSDs of wake centers tend to show better agreement at lower frequencies ($f_s < St_{in}$), which the POD modes in ROMs capture more accurately. Coherence decreases at higher frequencies, but because wake meandering is predominantly a low-frequency phenomenon, this reduction in coherence at higher $f_s$ is acceptable for the purposes of this study. Fig. 18 highlights the average coherence across the full frequency range for several cases. Good agreement between $S_{\mu\mu}$ and $S_{\hat{\mu}\hat{\mu}}$ is observed, particularly for $x/D > 4$. Highlighted regions in Fig. 18 show where $f_s > St_{in}$, corresponding to reduced frequencies above the inflow Strouhal number, that are not typically associated with wake meandering.

Focusing on specific frequency ranges of $C_{\mu\hat{\mu}}$ provides a more accurate evaluation of each ROM's ability to reproduce wake meandering. High-frequency spectra are irrelevant for this analysis, as they do not reflect the physics of wake meandering. We evaluate the trends for ROMs in Fig. 18 by calculating the average coherence, $\overline{C}_{\mu\hat{\mu}}$, over the respective frequency ranges.

A more complete assessment of ROM quality appears in Fig. 19, which shows the average coherence over the reduced frequency, $\overline{C}\mu\hat{\mu}$. The top subfigure displays $\overline{C}_{\mu\hat{\mu}}$ for the full frequency range, with an average coherence of approximately 0.3 for most cases. The bottom subfigure, restricted to $f_s \leq St_{in}$, reveals more consistent results across blocks of ROMs. Referring to the mode distribution in each ROM shown in the combination tree (Fig. 17), a clear correlation emerges between $\overline{C}_{\mu\hat{\mu}}$ and the inclusion of specific modes.

Fig. 19 also reveals the dependence of $\overline{C}_{\mu\hat{\mu}}$ on the downstream distance from the lidar, as indicated by the vertical axes. By averaging along the range coordinate, we aggregate this information into a single scalar metric for each ROM, $\varepsilon = \langle \overline{C}_{\mu\hat{\mu}} \rangle$, where the angle brackets denote averaging along the streamwise coordinate. This allows us to describe the ROM distribution with a quantitative fit quality metric. Fig. 20 (left) shows $\varepsilon$ arranged by ROM index across the 16,278 mode combinations. The data in Fig. 20 reflect the same information as Fig. 19, averaged over the vertical axis (streamwise coordinate). On the right side of Fig. 20, the distribution of ROM quality is shown according to the number of modes used in each ROM. Although including more modes generally improves the representation of wake meandering, several exceptions to this trend exist. The distributions in Fig. 20 (right) show that some ROMs with only four modes outperform others with 10 or more modes.

To investigate the sensitivity of wake center coherence to POD modes, we use an Analysis of Variance (ANOVA) approach [51]. We

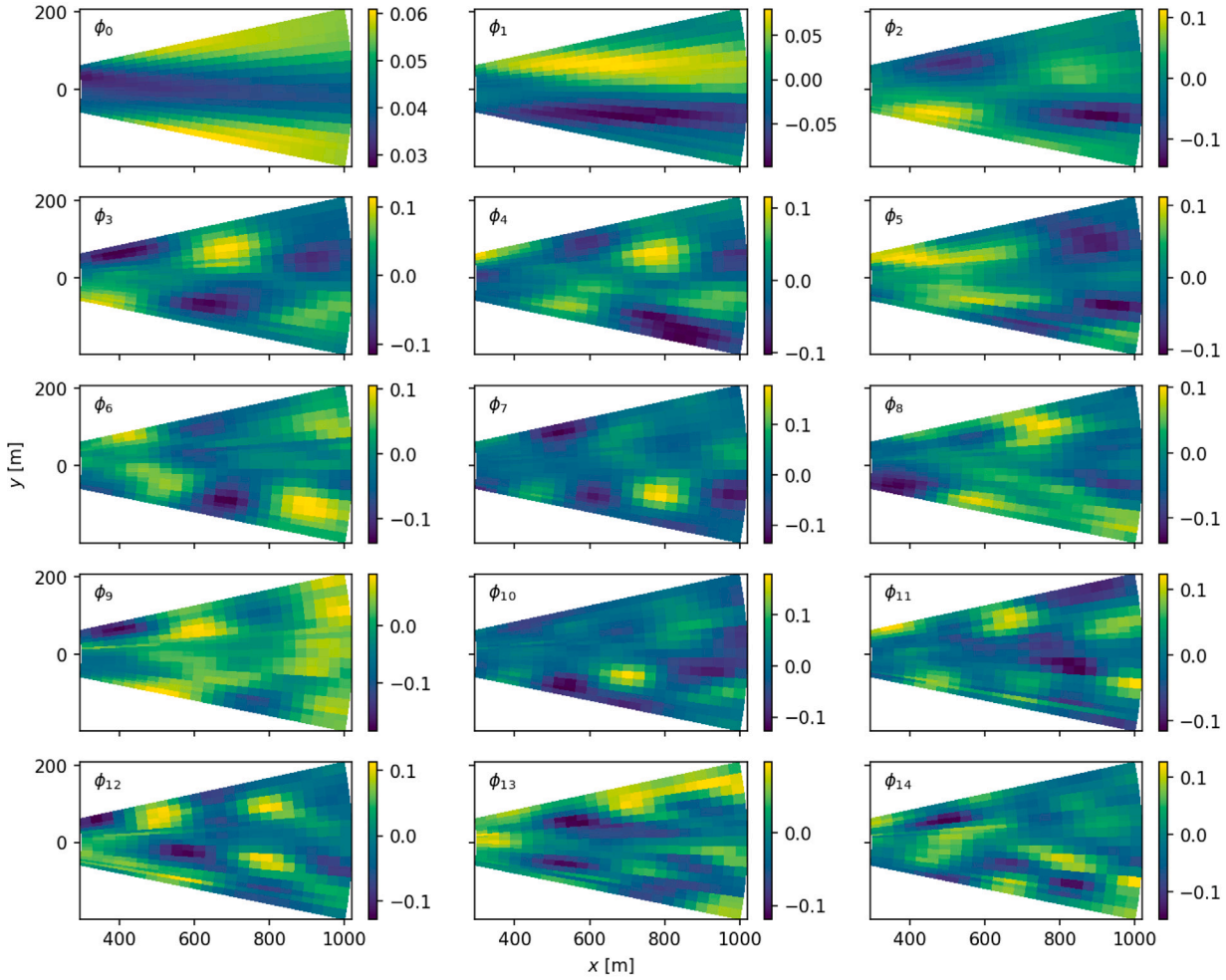


**Fig. 16.** POD modes from the example case on 2023-09-04 10:30 UTC.

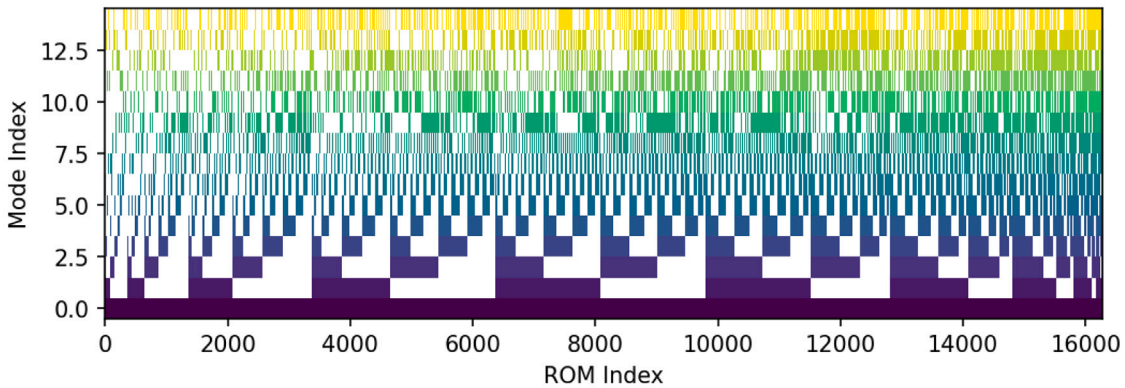


**Fig. 17.** Combination tree indicating which modes are contained in any given ROM. Modes are indicated by the colored regions, and their absence is shown in white.

develop a statistical model to decompose the average coherence into contributions from individual modes and their interactions. The model takes the following linear decomposition form, where $\varepsilon$ is the average coherence, a quality metric for each ROM:

$$\varepsilon = \bar{\varepsilon} + \sum_{i=1}^{n} \beta_i q_i + \sum_{i<j}^{n} \gamma_{ij} q_i q_j + \xi \tag{19}$$

Here, $\bar{\varepsilon}$ represents the mean coherence of all 16,278 ROMs per case, $\beta_i$ are the main effects of individual modes, and $\gamma_{ij}$ capture the interaction effects between modes. The binary variables $q_i$ indicate the presence (1) or absence (0) of each mode, with the constraint that at least three modes must be included. The term $\xi$ represents the residual error, describing noise not accounted for in the model in Eq. (19).

We impose statistical constraints, assuming that both the main effects $\beta_i$ and interaction terms $\gamma_{ij}$ follow a normal distribution with zero mean, and that the residual error $\xi$ follows a normal distribution. The goal is to estimate the coefficients $\beta_i$ and $\gamma_{ij}$ that minimize the residual error and provide insight into how modes and their combinations influence wake center coherence. This approach allows for a comprehensive sensitivity analysis, capturing the complex, potentially

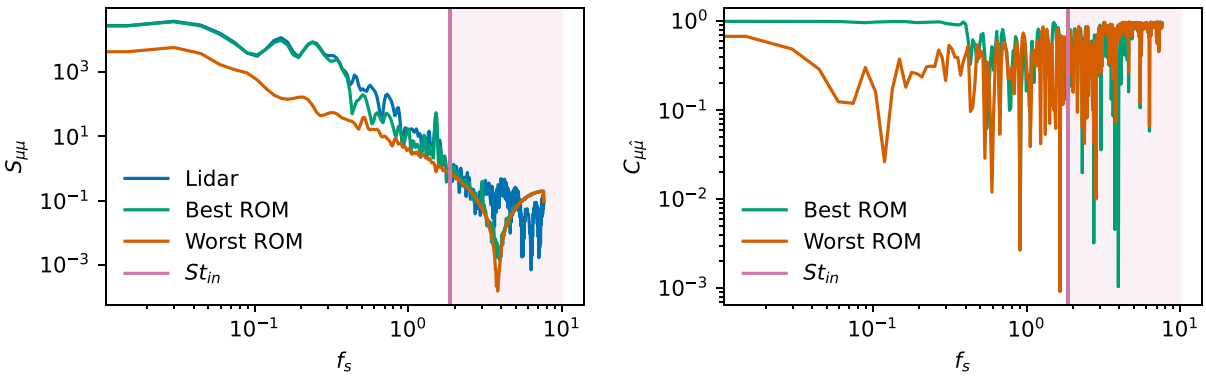


**Fig. 18.** Spectra (left) and coherence (right) for the ROMs that compare best (green) and worst (orange) to the PSD of $\mu$ from the lidar scans.

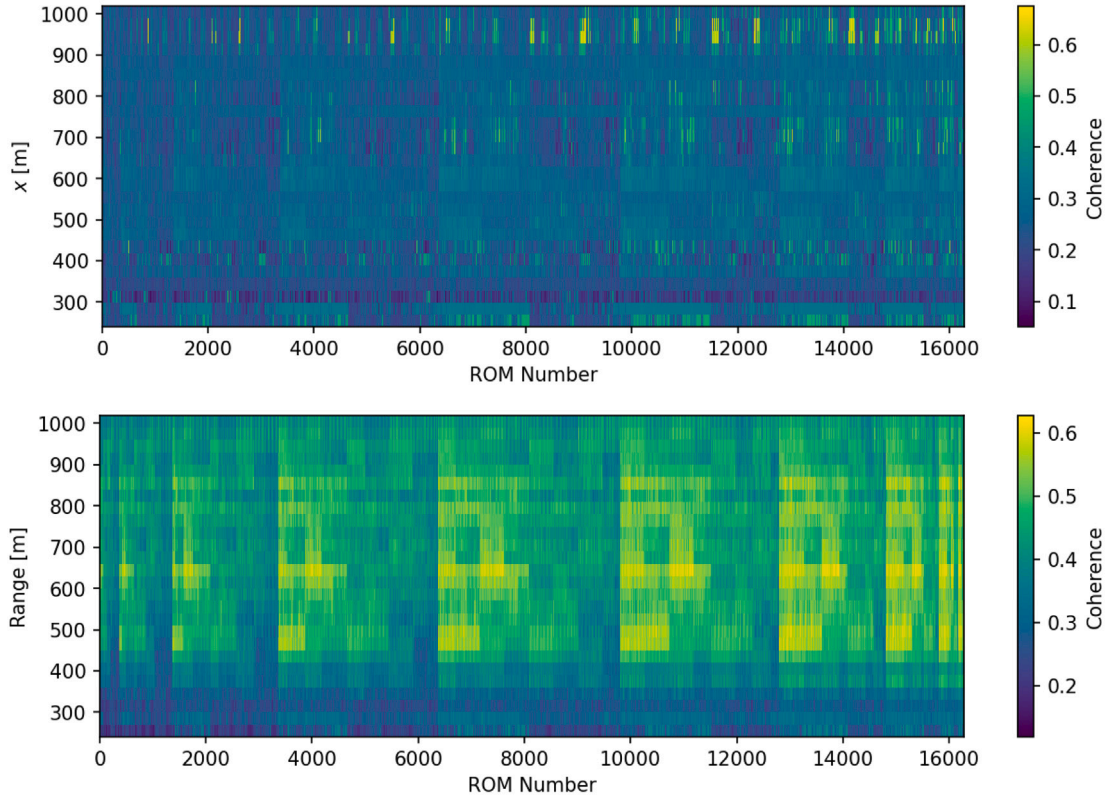


**Fig. 19.** Frequency-averaged coherence between detected wake centers from lidar scans and ROMs considering the full measured frequency range (top) and only frequencies $f_s \leq St_{in}$ Hz (bottom).

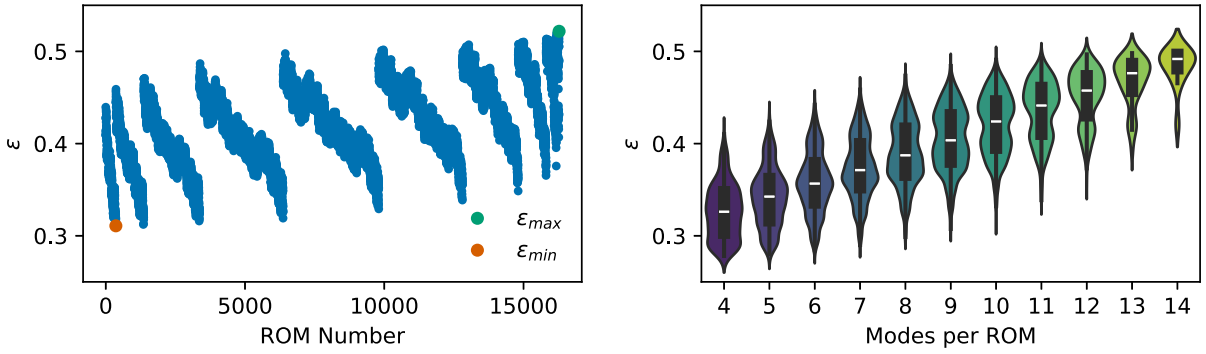


**Fig. 20.** Frequency- and range-averaged coherence between detected wake centers from lidar scans and ROMs considering $f_s \leq St_{in}$ Hz (left). Distribution of $\epsilon$ by the number of modes contained in each ROM (right).

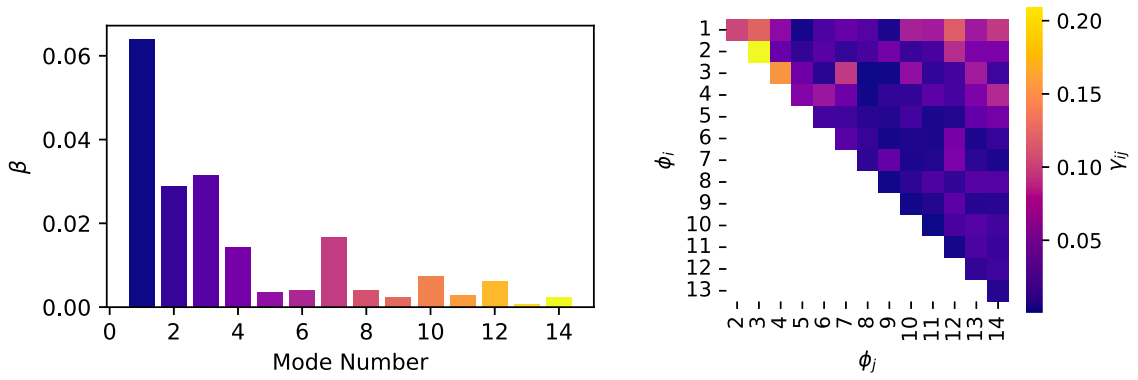


**Fig. 21.** Main effect $\beta_i$ of each mode and interaction effects $\gamma_{ij}$ between modes building the linear system that describes the dependence of average coherence on the presence or absence of each mode.

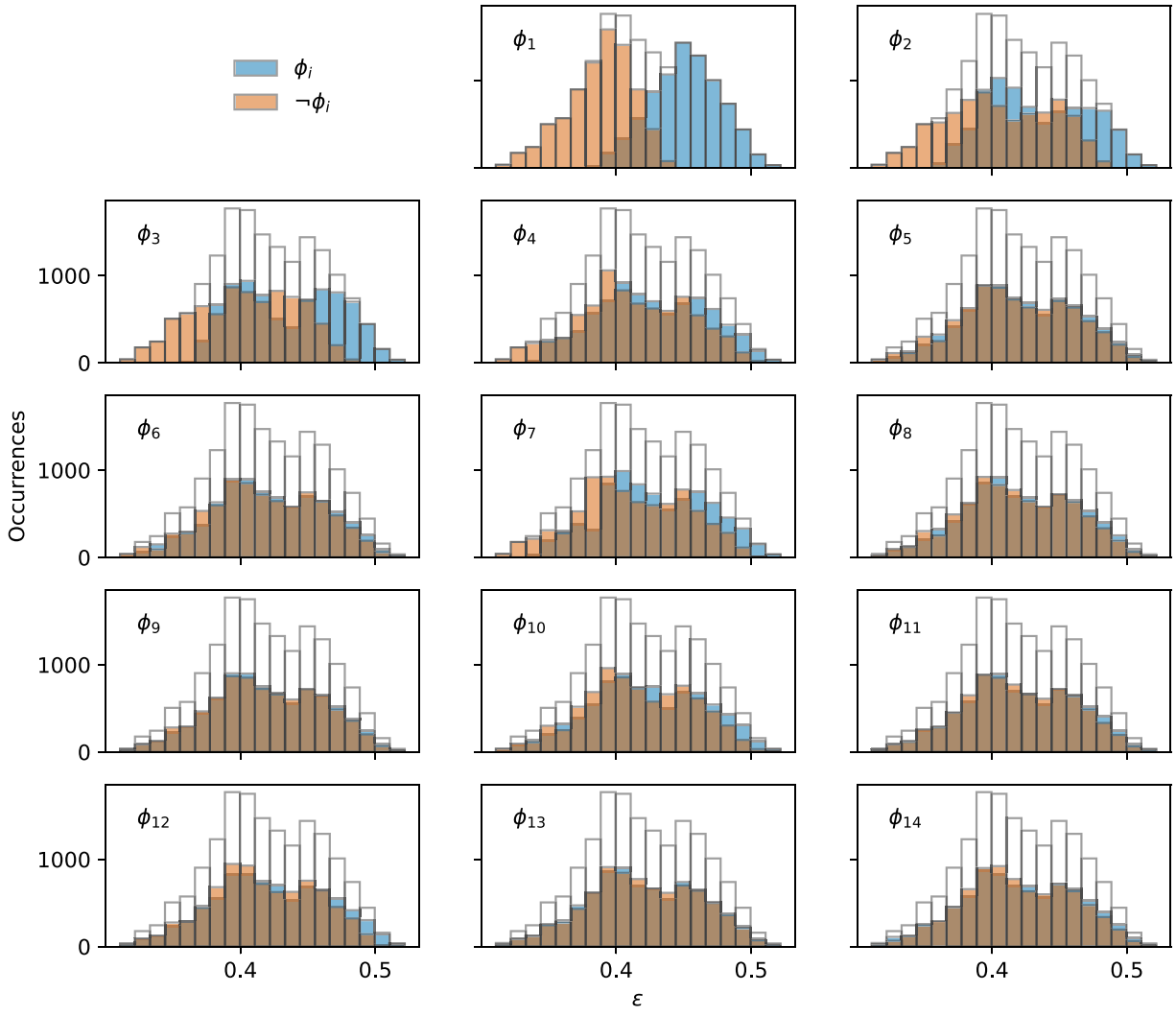


**Fig. 22.** Distributions of $\varepsilon$ consider ROMs that include each mode (blue) or exclude each mode (orange).

nonlinear interactions between POD modes in representing wake center dynamics.

Fig. 21 (right) shows the main effects $\beta_i$ of each mode for the case beginning at 2023-09-04 10:30 UTC, the same case used to illustrate the POD modes above. One key finding illustrated by this figure is that the importance of each mode does not decay monotonically with the mode index. This indicates that although certain modes may represent more TKE in the full basis, they do not necessarily have a greater impact on wake meandering. Instead, the modes that exhibit asymmetrical structure across the wake centerline also tend to have the largest values of $\beta_i$. The magnitude of the mode coefficients is small, $\beta \lesssim 0.1$, due to the bounded range of the average ROM coherence, $0.3 < \varepsilon < 0.55$.

To illustrate the importance of each mode more completely, Fig. 22 splits the full distribution of $\varepsilon$ (in white) into subsets of ROMs that include (blue) or exclude (orange) each of the first 14 modes. Modes with the strongest impact on $\varepsilon$ (i.e., modes 1, 2, 3) show the greatest

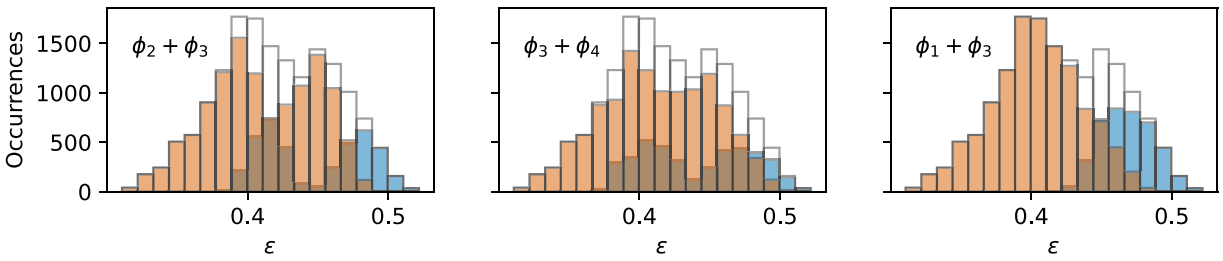


**Fig. 23.** Distributions of the average coherence for ROMs that include or exclude the indicated pairs of modes listed in descending order of importance. For each mode pair, from left to right, $\gamma_{2,3} = 0.209$, $\gamma_{3,4} = 0.157$, and $\gamma_{1,3} = 0.125$.

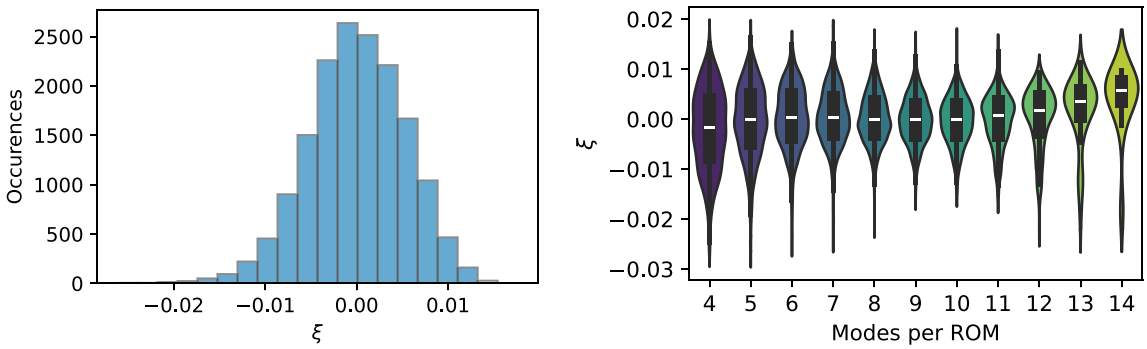


**Fig. 24.** Normal distribution of the ANOVA residual error, $\xi$ (left), and residual error aggregated by the number of modes in each ROM (right).

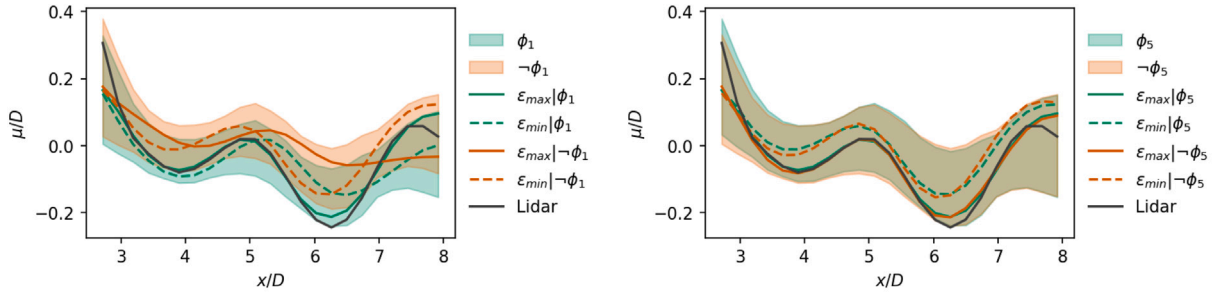


**Fig. 25.** Wake centers for a single stamp comparing observations from the lidar (black) and centers estimated with (green) and without (orange) $\phi_1$ (left) and $\phi_5$ (right).

separation between distributions of ROMs that include or exclude $\phi_i$. Moreover, ROMs that contain the modes that have the greatest positive impact on $\varepsilon$ always show distributions with means greater for ROMs that that exclude $\phi_i$. Conversely, distributions for modes with little influence on $\varepsilon$ (e.g., modes 9, 11, 13) are nearly identical for ROMs that include or exclude the modes.

The case at 2023-09-04 10:30 UTC also exhibits relatively large mode interaction effects between a few particular mode pairs, as shown in Fig. 21 (right). In particular, $\varepsilon$ shows a strong colinear dependence on modes 2 and 3, modes 3 and 4, and modes 1 and 3, in descending order. Fig. 23 compares the distribution of $\varepsilon$ for ROMs containing both modes in the pair $(\phi_i + \phi_j)$ against that for ROMs not containing both modes $\neg(\phi_i + \phi_j)$, including those that contain only one of the modes of interest. Interestingly, the distribution of $\varepsilon$ for the pair $\phi_1 + \phi_3$ (right) is roughly normal, while for mode pairs $\phi_2 + \phi_3$ and $\phi_3 + \phi_4$ (left and center), the distributions are strongly bimodal.

Verifying one of the key assumptions that underpins the ANOVA described by Eq. (19), the residual $\xi$, shown in Fig. 24 (left), is roughly normally distributed. The range of $\xi$ is relatively small, with a standard deviation of $\sigma_{\bar{\xi}} \approx 0.003$, although the main effect $\beta_i$ of some less relevant modes falls within the range of the residual. Fig. 24 (right) also shows that the distributions of $\xi$, aggregated by the number of modes used to compose a ROM, are approximately normally distributed. Distributions of ANOVA residual error appear to be consistently centered around $\xi = 0$, except for ROMs with 4 modes where there is a slight negative bias, and ROMs with more than 11 modes for which there is a slight positive bias. Recalling that the sample size of ROMs composed with a given number of modes varies (Fig. 1), the distributions for ROMs composed with fewer than 4 or more than 11 modes are not necessarily statistically converged. Distributions of ROMs composed with between 6 and 10 modes contain at least 1000 samples, suggesting that they represent distributions of $\xi$ more accurately.

To illustrate the range of ROM accuracy, Fig. 25 compares detected wake centers from the lidar directly to the low-order descriptions provided by selected modes. Specifically, Fig. 25 highlights the ROMs with the maximum (solid colored lines) and minimum values (dashed colored lines) of $\varepsilon$, that is, the ROMs that have wake center dynamics that show the maximum and minimum average correlation with the lidar observations. The importance of the presence or absence of either $\phi_1$ or $\phi_5$ (left and right, respectively) is highlighted by comparing the colored traces indicating the wake centers predicted by the ROMs. In the case of the first mode (with a large $\beta$ coefficient), the trace for $\varepsilon_{\max}|\phi_1$ (solid green line) case is nearly identical to the wake centers observed with the lidar. In the absence of the first mode, the best case of $\varepsilon_{\max}|\neg\phi_1$ (solid orange line) shows meandering with a much smaller amplitude than expected. Looking toward the fifth mode, the best and worst cases are nearly indistinguishable considering ROMs with and without $\phi_5$, visually demonstrating the lack of dependence of $\varepsilon$ on $\phi_5$.

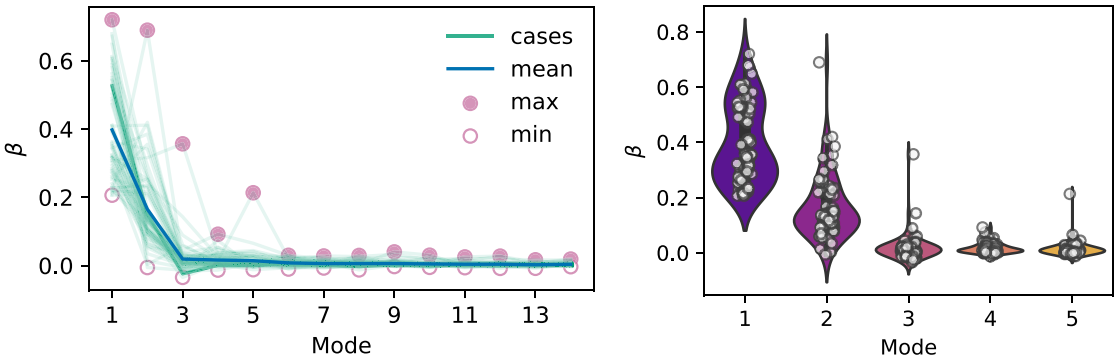


**Fig. 26.** Trends of $\beta$ considering all 65 cases in the overall study.

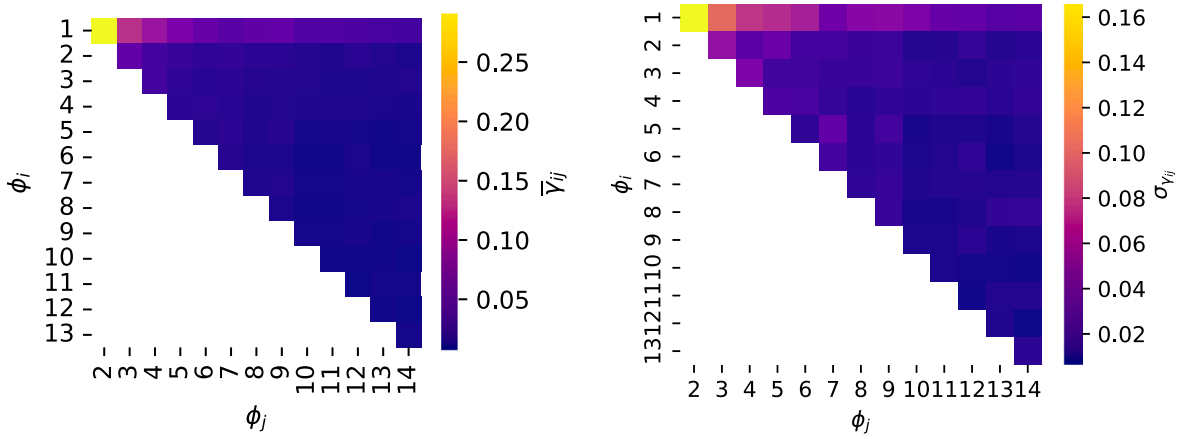


**Fig. 27.** Trends of $\overline{\gamma}_{ij} = f(\phi_i, \phi_j)$ considering all 65 cases in the overall study.

For both examples, the shaded region indicates the range of $\hat{\mu}$ given either the presence (green) or absence of the respective mode.

Considering the full population of 65 cases considered in this study, Fig. 26 shows the overall trends of $\beta$ with mode index. The mean profile in blue indicates that the first mode tends to contribute quite strongly to the linear model of $\epsilon$, with a coefficient of $\beta_1 = 0.4$. In most cases, the mode $\phi_1$ is qualitatively similar to that shown for 2023-09-04 10:30 UTC in Fig. 16, exhibiting a strongly antisymmetric character along the average wake centerline and a half-period of streamwise variation. Fig. 26 indicates that this mode can account for a huge amount of $\epsilon$, ranging from a coefficient of $0.2 \leq \beta_1 \leq 0.75$, as shown by the pink lines indicating maximum and minimum values.

The range of $\phi_2$ is even larger, showing a maximum value of $\beta_2 = 0.72$, similar to that of $\beta_1$, while the minimum value is $\beta_2 = -0.02$, indicating that for some cases, the average correlation $\epsilon$ is weakly anticorrelated with mode $\phi_2$. Similar behavior is evident for modes $\phi_2$ through $\phi_8$, where at least the modes work against the successful representation of $\epsilon$ for several cases.

Fig. 26 (right) shows the distributions of $\beta_0$ through $\beta_4$ in greater detail as violin plots with markers indicating values for individual cases. Overall, the figure suggests a trend of decreasing range of $\beta$ as the mode increases. Modes 1, 2, and 4 show what appear to be outlier values extending the range to higher positive values of $\beta$. Mode 0 also appears to have a bimodal distribution of $\beta$. Because there are only 65 cases in the current study, and those cases span a wide range of atmospheric conditions, insights drawn from the relationship between $\epsilon$ and $\beta_i$ should be treated with an appropriate level of caution.

The description of multi-colinear dependence of $\epsilon$ on the modal basis $\phi_i$ has a similar trend. Fig. 27 shows the mean (left) and standard deviation (right) of $\gamma_{ij}$ for the collection of 65 cases. Overall, $\phi_1$ has the strongest colinear behavior with the other modes in the basis, with a maximum value of $\overline{\gamma}_{1,2} = 0.29$ and decreasing monotonically with $j$ thereafter. The average colinear dependence of higher-order modes is even lower, suggesting that the global behavior for $\epsilon$ may be that a purely linear relationship is sufficient for description of wake meandering. The standard deviation of $\sigma_{\gamma_{ij}}$ shows similar trends as the mean, where the largest values are located in the top left, for colinearity between $\phi_1$ and $\phi_2$, decreasing as both $i$ and $j$ increase.

While the average behavior of $\beta$ suggests a monotonic decrease in value mode index, the true relationship is likely more complex and probably depends on the nature of the POD modes (symmetry, sequencing, etc.) representing wake dynamics for each case. Fig. 28 compares the log of the mode eigenvalues, $\log_{10}(\lambda_i)$ to the main effect coefficients $\beta_i$, colored by the mode number. Because $\beta_i$ tends toward zero for all cases while $\lambda_i$ show a wide range of values for each mode, no direct relationship between the two is directly evident in the current data. This disparity is thought to arise from the fact that the two variables describe related but different phenomena. POD modes describe the variance-maximizing structures in the observational basis; that is, they describe the TKE in the measurement domain of the nacelle-mounted scanning lidars—the eigenvalues $\lambda_i$ quantify the TKE each mode represents in the overall budget. The main effect coefficients, $\beta_i$, describe the dependence of the streamwise-averaged and reduced frequency-averaged correlation between wake centers estimated by a Gaussian function fit to the observational data and estimates made by a ROM as described by a subset of POD modes.

While the main effect coefficients do not appear to be correlated with the POD eigenvalues, there is a stronger connection with the mode symmetry, described in Eq. (17). Fig. 29 compares $\beta_i$ to the cosine distance that quantifies mode symmetry, $\kappa(\phi_i)$. Because the momentum deficit of the wake for each case is approximately symmetric along $y/D = 0$, the associated cosine distance $\kappa(\phi_0) \approx 1$ for all cases. The

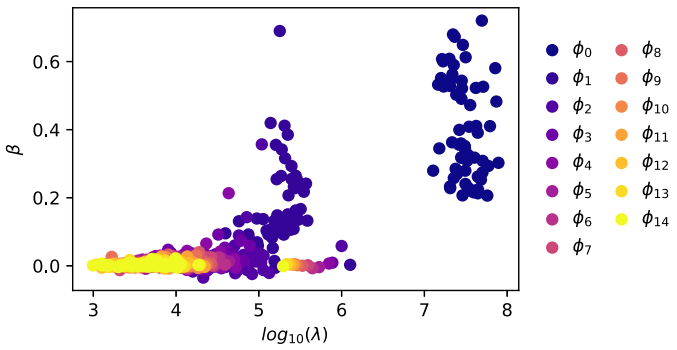


**Fig. 28.** Comparison of POD mode eigenvalues $\lambda_i$ to main effect coefficients $\beta_i$ for all 65 cases.

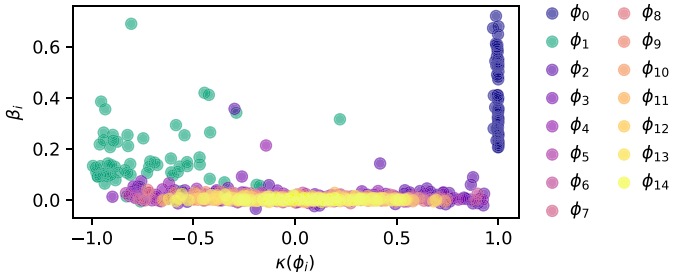


**Fig. 29.** Comparison of the mode symmetry $\kappa(\phi_i)$ to main effect coefficients $\beta_i$ for all 65 cases.

first mode tends to contain the most important contribution to wake meandering, and is also the most strongly antisymmetric, as indicated by the large negative values of $\kappa(\phi_1)$ (green markers). Other modes, which exhibit a wide range of $\kappa(\phi_i)$, are less important in the prediction of wake meandering.

The data in Figs. 28 and 29 suggest that the relevance of POD modes to wake meandering can be described based on their intrinsic characteristics. Mode symmetry, and to a lesser extent the TKE captured by each mode, allows us to estimate the significance of individual modes for the physics of wake meandering, independent of inflow conditions. However, this description remains phenomenological rather than causal or predictive. Fig. 30 connects the aggregate mode effect coefficients, $\sum_i \beta_i$, to inflow characteristics collected from the meteorological towers and surface stations in the AWAKEN and RAAW campaigns. Instead of analyzing individual mode effects, this approach aggregates the coefficients to provide a general measure of the predictive capability of the POD-based ROMs for wake meandering.

The results in Fig. 30 indicate that the aggregate mode effect coefficients correlate strongly with the integral timescale and turbulence intensity (TI) of the inflow (Fig. 30, left). The data show that the POD basis is more predictive of wake meandering in cases with low TI and large integral timescales. In contrast, for cases with moderate or high inflow turbulence (TI > 7%), the ROM's predictive accuracy diminishes. The center panel of Fig. 30 examines the relationship between the aggregate mode effect coefficient, the inflow Strouhal number, and the friction velocity $u_* = (\overline{u'w'}^2 + \overline{v'w'}^2)^{1/4}$. The analysis reveals an anticorrelation between the ROMs' effectiveness and both the Strouhal number and friction velocity. This suggests that the predictive capability of the modal basis decreases as these metrics increase. The right panel of Fig. 30 explores the relationship between the aggregate mode effect coefficient and surface-layer exchanges that quantify atmospheric stability. While $\sum_i \beta_i$ shows weaker correlations with the sensible heat flux, $q_s = \rho C_p \overline{w'\theta'}$, and momentum flux, $\tau_s = \rho(\overline{u'w'}^2 + \overline{v'w'}^2)^{1/2}$, the data suggest that POD modes are more predictive of wake meandering under near-neutral conditions when turbulent transport of momentum approaches zero. Pearson correlation coefficients between the aggregate mode effect coefficients and the key inflow quantities are listed in Table 3.

**Table 3**
Pearson correlation coefficient between the aggregate mode effect coefficients and key atmospheric characteristics.

| | Variable | Correlation strength |
|---|---|---|
| Integral timescale | $T_{int}$ | 0.74 |
| Turbulence intensity | TI | −0.70 |
| Friction velocity | $u_*$ | −0.68 |
| Momentum flux | $\tau_s$ | 0.62 |
| Inflow Strouhal number | $St_{in}$ | −0.60 |
| Sensible heat flux | $q_s$ | 0.45 |

## 5. Conclusions

This study leverages remote sensing data from nacelle-mounted scanning lidars to quantify wake meandering using snapshot POD and spectral methods. We find that the statistics of wake meandering differ across test cases, revealing significant insights into the spatiotemporal and spectral characteristics of wake dynamics. Our analysis of POD modes challenges conventional descriptions of wake meandering and its expected relationships with atmospheric inflow.

While low-order modes capture the largest, most energetic turbulent structures, these modes do not necessarily contribute the most to accurately representing wake meandering. Some modes show no correlation with meandering dynamics, and others distort or detract from an accurate representation of wake behavior. This finding suggests that certain modes are either irrelevant to wake meandering or are only regionally relevant. Importantly, the relevance of modes appears to depend on their symmetry and the amount of TKE they contain, as well as their connection to inflow characteristics such as turbulence intensity and integral timescales.

These results indicate that cases with low turbulence intensity and large integral timescales yield stronger correlations between POD modes and wake meandering, while cases with moderate or high inflow turbulence (TI > 7%) are less effectively captured by the ROM. Moreover, wake meandering models based on aggregated modal coefficients are anticorrelated with friction velocity and inflow Strouhal number, suggesting that the predictive strength of the modal basis is not easily deduced by characteristics of the inflow turbulence. These insights highlight the complex and multifaceted relationship between wake meandering and atmospheric dynamics, which current passive tracer or coherent structure interaction models fail to fully describe.

Although the POD modes describing wake dynamics differ quantitatively from case to case, they exhibit a qualitative similarity across a wide range of atmospheric conditions. This suggests the existence of a semi-universal basis of functions or structures that describe wind turbine wakes. We hypothesize that a low-dimensional manifold may exist, capable of efficiently and computationally representing wake aerodynamics and meandering, with potential benefits for steady-state and engineering models of wind turbine and wind plant wakes.

While this study provides a phenomenological description of wake meandering and its relationship with turbulent structures, it does not constitute a dynamic or predictive model. One key limitation is the difficulty in separating azimuthal wake position changes from yaw-induced turbine activity from the underlying wake dynamics. To address this, future studies could apply classical POD or dynamic mode decomposition to time series of estimated wake centers. Incorporating additional inflow dynamics and turbine operating states into such analyses could enable the development of a comprehensive dynamical model for wake centerline trajectories, including wake meandering.

By bridging these gaps, future work has the potential to advance predictive capabilities and improve the representation of wake dynamics in wind energy research and engineering applications.

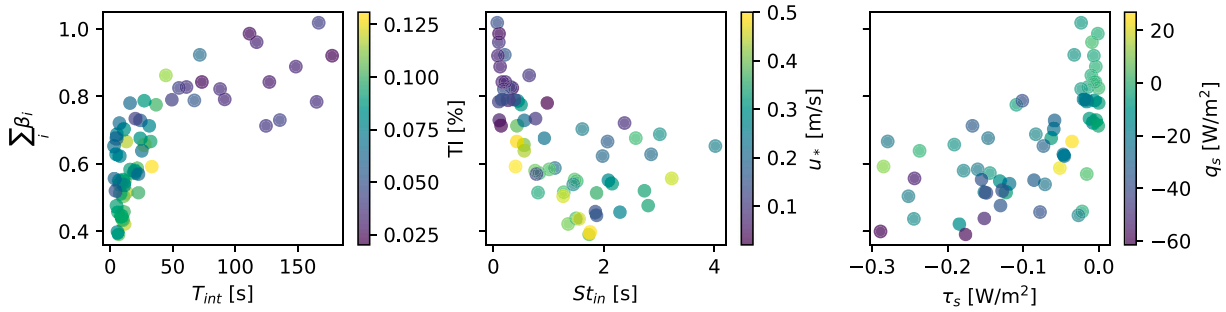


**Fig. 30.** Comparison of $\beta_i$ to $T_{int}$ colored by the turbulence intensity (TI) (left), to $St_{in}$ colored by the vertical velocity variance (center), and to the mean momentum flux colored by the sensible heat flux (right).

## CRediT authorship contribution statement

**Nicholas Hamilton:** Writing – review & editing, Writing – original draft, Visualization, Validation, Software, Project administration, Methodology, Investigation, Formal analysis, Data curation, Conceptualization. **Paula Doubrawa:** Writing – review & editing, Project administration, Funding acquisition, Conceptualization. **Patrick Moriarty:** Writing – review & editing, Project administration, Funding acquisition. **Stefano Letizia:** Writing – review & editing, Methodology, Data curation, Conceptualization. **Regis Thedin:** Writing – review & editing, Methodology, Formal analysis, Data curation, Conceptualization.

## Declaration of competing interest

The authors declare that they have no known competing financial interests or personal relationships that could have appeared to influence the work reported in this paper.

## Acknowledgments

This work was authored by the National Renewable Energy Laboratory, United States, operated by Alliance for Sustainable Energy, LLC, for the U.S. Department of Energy (DOE) under Contract No. DE-AC36-08GO28308. Funding provided by the U.S. Department of Energy Office of Energy Efficiency and Renewable Energy Wind Energy Technologies Office, United States. The views expressed herein do not necessarily represent the views of the DOE or the U.S. Government. The U.S. Government retains and the publisher, by accepting the article for publication, acknowledges that the U.S. Government retains a nonexclusive, paid-up, irrevocable, worldwide license to publish or reproduce the published form of this work, or allow others to do so, for U.S. Government purposes.

## References

[1] G.C. Larsen, H.A. Madsen, K. Thomsen, T.J. Larsen, Wake meandering: a pragmatic approach, Wind. Energy: Int. J. Prog. Appl. Wind. Power Convers. Technol. 11 (4) (2008) 377–395.

[2] A.S. Wise, E.E. Bachynski, Wake meandering effects on floating wind turbines, Wind. Energy 23 (5) (2020) 1266–1285, http://dx.doi.org/10.1002/we.2485, URL https://onlinelibrary.wiley.com/doi/abs/10.1002/we.2485.

[3] G. Espana, S. Aubrun, S. Loyer, P. Devinant, Wind tunnel study of the wake meandering downstream of a modelled wind turbine as an effect of large scale turbulent eddies, J. Wind Eng. Ind. Aerodyn. 101 (2012) 24–33.

[4] R.W. Baker, S.N. Walker, Wake Velocity Deficit Measurements at the Goodnoe Hills MOD-2 Site: A Summary of the 1982 and 1984 Findings, Tech. Rep., Oregon State Univ., Corvallis (USA). Wind Resources Assessment Lab., 1985.

[5] T. Zambrano, G. Gyatt, Wake structure measurements at the MOD-2 cluster test facility at goodnoe hills, washington, IEE Proc. A (Phys. Sci. Meas. Instrum. Manag. Educ. Rev.) 130 (9) (1983) 562–565.

[6] D. Medici, P.H. Alfredsson, Measurements behind model wind turbines: further evidence of wake meandering, Wind. Energy: Int. J. Prog. Appl. Wind. Power Convers. Technol. 11 (2) (2008) 211–217.

[7] V. Okulov, J.N. Sørensen, Stability of helical tip vortices in a rotor far wake, J. Fluid Mech. 576 (2007) 1–25.

[8] K.B. Howard, A. Singh, F. Sotiropoulos, M. Guala, On the statistics of wind turbine wake meandering: An experimental investigation, Phys. Fluids 27 (7) (2015) 075103.

[9] D. Foti, X. Yang, F. Campagnolo, D. Maniaci, F. Sotiropoulos, Wake meandering of a model wind turbine operating in two different regimes, Phys. Rev. Fluids 3 (5) (2018) 054607.

[10] S.J. Andersen, J.N. Sørensen, R. Mikkelsen, Simulation of the inherent turbulence and wake interaction inside an infinitely long row of wind turbines, J. Turbul. 14 (4) (2013) 1–24.

[11] Z. Li, G. Dong, X. Yang, Onset of wake meandering for a floating offshore wind turbine under side-to-side motion, J. Fluid Mech. 934 (2022) A29, http://dx.doi.org/10.1017/jfm.2021.1147.

[12] F. Bingöl, J. Mann, G.C. Larsen, Light detection and ranging measurements of wake dynamics part I: one-dimensional scanning, Wind. Energy 13 (1) (2010) 51–61.

[13] G.C. Larsen, H. Aagaard Madsen, F. Bingöl, Dynamic wake meandering modeling, 2007.

[14] P. Brugger, M. Debnath, A. Scholbrock, P. Fleming, P. Moriarty, E. Simley, D. Jager, J. Roadman, M. Murphy, H. Zong, et al., Lidar measurements of yawed-wind-turbine wakes: characterization and validation of analytical models, Wind. Energy Sci. 5 (4) (2020) 1253–1272.

[15] S. Letizia, P. Brugger, N. Bodini, R. Krishnamurthy, A. Scholbrock, E. Simley, F. Porté-Agel, N. Hamilton, P. Doubrawa, P. Moriarty, Characterization of wind turbine flow through nacelle-mounted lidars: a review, Front. Mech. Eng. 9 (2023) 1261017.

[16] E. Simley, H. Fürst, F. Haizmann, D. Schlipf, Optimizing Lidars for wind turbine control applications—Results from the IEA wind task 32 Workshop, Remote Sens. 10 (6) (2018) 863.

[17] M. Pichault, C. Vincent, G. Skidmore, J. Monty, Short-term wind power forecasting at the wind farm scale using long-range Doppler lidar, Energies 14 (9) (2021) 2663.

[18] N. Bodini, D. Zardi, J.K. Lundquist, Three-dimensional structure of wind turbine wakes as measured by scanning lidar, Atmospheric Meas. Tech. 10 (8) (2017) 2881–2896.

[19] D. Conti, N. Dimitrov, A. Peña, T. Herges, Calibration and validation of the Dynamic Wake Meandering model Part I: Bayesian estimation of model parameters using SpinnerLidar-derived wake characteristics, Wind. Energy Sci. Discuss. (2021) 1–39.

[20] I. Reinwardt, L. Schilling, P. Dalhoff, D. Steudel, M. Breuer, Dynamic wake meandering model calibration using nacelle-mounted lidar systems, Wind. Energy Sci. 5 (2) (2020) 775–792.

[21] D. Conti, N. Dimitrov, A. Peña, T. Herges, Wind turbine wake characterization using the SpinnerLidar measurements, J. Phys.: Conf. Ser. 1618 (2020) 062040.

[22] P. Doubrawa, E.W. Quon, L.A. Martinez-Tossas, K. Shaler, M. Debnath, N. Hamilton, T.G. Herges, D. Maniaci, C.L. Kelley, A.S. Hsieh, et al., Multimodel validation of single wakes in neutral and stratified atmospheric conditions, Wind. Energy 23 (11) (2020) 2027–2055.

[23] G. Berkooz, P. Holmes, J.L. Lumley, The proper orthogonal decomposition in the analysis of turbulent flows, Annu. Rev. Fluid Mech. 25 (1) (1993) 539–575.

[24] K. Saranyasoontorn, L. Manuel, Low-dimensional representations of inflow turbulence and wind turbine response using proper orthogonal decomposition, J. Sol. Energy Eng. 127 (4) (2005) 553–562.

[25] N. Hamilton, M. Tutkun, R.B. Cal, Low-order representations of the canonical wind turbine array boundary layer via double proper orthogonal decomposition, Phys. Fluids 28 (2) (2016) 025103.

[26] N. Coudou, S. Buckingham, L. Bricteux, J. van Beeck, Experimental study on the wake meandering within a scale model wind farm subject to a wind-tunnel flow simulating an atmospheric boundary layer, Bound.-Layer Meteorol. 167 (2018) 77–98.

[27] M. Heisel, J. Hong, M. Guala, The spectral signature of wind turbine wake meandering: A wind tunnel and field-scale study, Wind. Energy 21 (9) (2018) 715–731.

[28] J.M. Jonkman, J. Annoni, G. Hayman, B. Jonkman, A. Purkayastha, Development of fast. farm: A new multi-physics engineering tool for wind-farm design and analysis, in: 35th Wind Energy Symposium, 2017, p. 0454.
[29] K. Shaler, J. Jonkman, P. Doubrawa Moreira, N. Hamilton, FAST. Farm Response to Varying Wind Inflow Techniques, Tech. Rep., National Renewable Energy Lab.(NREL), Golden, CO (United States), 2019.
[30] L. Zhan, S. Letizia, G. Valerio Iungo, Lidar measurements for an onshore wind farm: Wake variability for different incoming wind speeds and atmospheric stability regimes, Wind. Energy 23 (3) (2020) 501–527.
[31] P. Holmes, Turbulence, Coherent Structures, Dynamical Systems and Symmetry, Cambridge University Press, 2012.
[32] P. Moriarty, N. Bodini, S. Letizia, A. Abraham, T. Ashley, K.B. Bärfuss, R.J. Barthelmie, A. Brewer, P. Brugger, T. Feuerle, et al., Overview of preparation for the American WAKE ExperimeNt (AWAKEN), J. Renew. Sustain. Energy 16 (5) (2024).
[33] C. Kelley, P. Doubrawa, N. Hamilton, J. Naughton, Rotor Aerodynamics, Aeroelastics, & Wake Project, Tech. Rep., Sandia National Lab.(SNL-NM), Albuquerque, NM (United States), 2022.
[34] Atmosphere to Electrons (A2e), Awaken/sa1.sonic.z01.b0, 2024, http://dx.doi.org/10.21947/1991104, https://a2e.energy.gov/data, Maintained by A2e Data Archive and Portal for U.S. Department of Energy, Office of Energy Efficiency and Renewable Energy.
[35] Atmosphere to Electrons (A2e), Awaken/kp.met.z01.a0, 2023, http://dx.doi.org/10.21947/2287629, https://a2e.energy.gov/data, Maintained by A2e Data Archive and Portal for U.S. Department of Energy, Office of Energy Efficiency and Renewable Energy.
[36] D.R. Cook, Eddy Correlation Flux Measurement System (ECOR) Instrument Handbook, Tech. Rep., DOE Office of Science Atmospheric Radiation Measurement (ARM) Program . . . , 2018.
[37] Atmosphere to Electrons (A2e), Raaw/ge.met.z01.b1, 2023, https://a2e.energy.gov/data, Maintained by A2e Data Archive and Portal for U.S. Department of Energy, Office of Energy Efficiency and Renewable Energy.
[38] Atmosphere to Electrons (A2e), Awaken/rt1.lidar.z02.a0, 2024, http://dx.doi.org/10.21947/1970311, https://a2e.energy.gov/data, Maintained by A2e Data Archive and Portal for U.S. Department of Energy, Office of Energy Efficiency and Renewable Energy.
[39] Atmosphere to Electrons (A2e), Raaw/nrel.lidar.z02.b0, 2023, https://a2e.energy.gov/data, Maintained by A2e Data Archive and Portal for U.S. Department of Energy, Office of Energy Efficiency and Renewable Energy.
[40] S. Letizia, L. Zhan, G.V. Iungo, Lisboa (LiDAR statistical barnes objective analysis) for optimal design of lidar scans and retrieval of wind statistics–part 2: Applications to lidar measurements of wind turbine wakes, Atmos. Meas. Tech. 14 (3) (2021) 2095–2113.
[41] NREL/FIEXTA, 2024, URL https://github.com/NREL/FIEXTA.
[42] H. Beck, M. K uhn, Dynamic data filtering of long-range Doppler LiDAR wind speed measurements, Remote. Sens. 9 (6) (2017) http://dx.doi.org/10.3390/rs9060561, URL https://www.mdpi.com/2072-4292/9/6/561.
[43] H. Beck, M. Kühn, Temporal Up-Sampling of Planar Long-Range Doppler LiDAR Wind Speed Measurements Using Space-Time Conversion, Remote. Sens. 11 (7) (2019-01) 867, http://dx.doi.org/10.3390/rs11070867, URL https://www.mdpi.com/2072-4292/11/7/867.
[44] J.-J. Trujillo, F. Bingöl, G.C. Larsen, J. Mann, M. Kühn, Light detection and ranging measurements of wake dynamics. Part II: two-dimensional scanning, Wind. Energy 14 (1) (2011) 61–75.
[45] M. Puccioni, M. Calaf, E.R. Pardyjak, S. Hoch, T.J. Morrison, A. Perelet, G.V. Iungo, Identification of the energy contributions associated with wall-attached eddies and very-large-scale motions in the near-neutral atmospheric surface layer through wind LiDAR measurements, J. Fluid Mech. 955 (2023) 1–40, http://dx.doi.org/10.1017/jfm.2022.1080, arXiv:2208.06908.
[46] N. Hamilton, Atmospheric condition identification in multivariate data through a metric for total variation, Atmos. Meas. Tech. 13 (2) (2020) 1019–1032.
[47] N.R.E. Laboratory, NREL 2.8-127 wind turbine model, 2022, https://github.com/NREL/openfast-turbine-models/tree/main/IEA-scaled/NREL-2.8-127. (Accessed 14 May 2025).
[48] M. Debnath, P. Brugger, E. Simley, P. Doubrawa, N. Hamilton, A. Scholbrock, D. Jager, M. Murphy, J. Roadman, J.K. Lundquist, P. Fleming, F. Porté-Agel, P. Moriarty, Longitudinal coherence and short-term wind speed prediction based on a nacelle-mounted Doppler lidar, J. Phys.: Conf. Ser. 1618 (2020) 032051, http://dx.doi.org/10.1088/1742-6596/1618/3/032051.
[49] A. Keane, Advancement of an analytical double-Gaussian full wind turbine wake model, Renew. Energy 171 (2021) 687–708.
[50] Z. Sadek, R. Scott, N. Hamilton, R.B. Cal, A three-dimensional, analytical wind turbine wake model: Flow acceleration, empirical correlations, and continuity, Renew. Energy 209 (2023) 298–309.
[51] H. Sahai, M.I. Ageel, The Analysis of Variance: Fixed, Random and Mixed Models, The Analysis of Variance, Springer Science & Business Media, 2012.